Dynamics of Laser-Induced Thin Film Machining Processes
(Lézeres vékonyrétegmegmunkálási folyamatok dinamikája)

PhD thesis
doktori disszertáció

Kántor Zoltán

Research Group on Laser Physics
MTA Lézerfizikai Tanszéki Kutatócsoport
Szeged, 1996.

General introduction

Year-by-year new and efficient laser sources leave the laboratory phase and break into industrial technologies, a continuously widening variety of wavelengths, pulse lengths and intensities are steadily calling for the application. Thus, adaptation and integration of the new sources into well established technologies and development of new applications prompt for intense R+D activity in the materials science.

Since the appearance of the first lasers in the 60's, practically all available materials have been exposed to laser radiation by the scientists. Due to the wide spectrum of the possible laser-induced processes from the simple thermal influence to photochemistry and the easy delivery of the laser beam (e.g. as compared to particle beam processing), laser assisted methods cover continuously expanding areas in materials processing. Although the development of smart materials is a big challenge, the appropriate shaping of them for practical purposes is a difficult technological problem as well. Shaping can be achieved by laser-induced removal of the unnecessary parts of the given material, furthermore, there exist certain laser techniques which can transfer or synthesize the given material in one step directly in the desired shape [1, 2, 3, 4, 5, 6, 7, 8].

Lasers can not only improve the efficiency and the quality of production processes which could also be done by traditional means, but a number of genuine techniques are based on the introduction of lasers. Under laser treatment, materials may respond unexpectedly: largely non-equilibrium processes due to fast heating and cooling rates, large gradients and — in thin film processing — boundary effects may lead to the appearance of extreme reaction speeds, transport phenomena and new metastable phases of materials. Furthermore, even reactions can be lead through unknown pathways. The characterization of the laser-induced processes is, therefore, usually difficult. The analysis of the final state of the material does not provide sufficient information about the diverse elemental steps of the overall laser-assisted process, which change the state of the material in the nanosecond time scale.

The acquisition of optical data is a reliable tool for following the events during laser processing: geometrical changes (bending, fragmentation, etc.), phase changes and chemical transformations in the material influence the optical properties of the surface. Some of the optical parameters, namely reflectivity, transmittance and scattering etc. can be measured easily even with high temporal resolution and spatial selectivity. Moreover, ultrafast photographic techniques are now able to record pictures of the transforming and moving material with exposition times as short as 1 ns.

Except for the case of direct photochemical processes, these changes are in correlation with the laser-induced temperature rise, as far as phase changes and deformations may occur, high temperatures and temperature gradients induce or enhance diffusion processes or enforce the onset of chemical reactions. As opposed to the optical characteristics, the temperature distribution in the material, practically, can not be measured during processing. The size and long response time of thermo-electric detectors (thermopiles, thermocouples, etc.) and opto-electric detectors (cooled Ge, CdS etc. crystals, e.g. for spectral temperature determination) is not appropriate for observing short-time scale transient heating in microscopic volumes.

As long as the laser-induced processes can be handled in the framework of heat conduction and first-order phase changes, the temperature profile, as a function of time, can be calculated numerically with fairly good reliability (in certain cases, the insufficient knowledge of the temperature-dependent thermophysical and optical properties, the

occurrence of difficult, unexpected or stochastic processes, changes of the material parameters due to non-equilibrium processes may cause strong limitations). Thus, because of its importance, the basic concepts of the numerical temperature calculation of laser-irradiated film-substrate systems are outlined in the Appendix.

In the present dissertation I summarize the main results of my work concerning surface patterning by laser-induced micromachining of thin film materials. Section 1. deals with laser induced transfer of thin films. Among other local thin film deposition techniques, Laser-Induced Forward Transfer appeared as a promising candidate in the mid 80's. Systematic investigation of this method has been performed and a critical analysis of nanosecond-pulse induced transfer experiments is given in Section 1.2. Although it was shown that such short laser pulses can not result in high quality transfer of thin metal films, the experiments enlightened several features of pulsed laser processing, such as the possibility of clean ablation of the films at rather low laser fluences or inhomogeneous melting over the illuminated area (Section 1.2.3.2.). In addition, the experiments revealed that the sub-millisecond pulse length range may be more suitable for the optimization of the process. This optimization work is detailed in Sections 1.3. and 1.4. First, in Section 1.3. the feasibility of good-quality transfer of metal patterns with long laser pulses is demonstrated. Further experiments were performed to understand and optimize the laser transfer process using real-time measurements of optical properties of the processed areas, and the results are presented in Section 1.4. For these experiments a μs-pulse laser microprocessing and monitoring system has been constructed in our laboratory.

As another application of this experimental arrangement, compound formation from stacked elemental layers was also examined with real-time optical measurements. Dynamics of laser-induced synthesis of zinc selenide is discussed in Section 2.

Section 3. deals with excimer laser-induced ablation of thin tin oxide and indium-tin oxide films from glass support. It is shown that, from one hand, clean ablation is typical not only of thin metal films but of practically all types of supported thin films; moreover, among the physical properties of the given materials, the ablation characteristics depend strongly on the initial film thickness. On the other hand, laser irradiation may induce chemical changes and/or structural rearrangement (incongruent ablation) within the material, which must be considered in specific applications.

Section 4., finally, summarizes the main results and conclusions.

1. Laser-Induced Transfer of thin films

1.1. Ablation and related phenomena

The importance of the freeing the substrate from the pre-deposited thin film over small areas or the formation of small holes by lasers was early recognized and several attempts have been done to introduce this technique into the fine optics, fine mechanics and micromechanics [9, 10, 11]. The change of the electrical properties of the surface upon ablation was of great potential in electronic applications. Some attempts for microelectronics application are mentioned e.g. in Refs. [12, 13, 14, 15]. On larger scales, pulsed laser trimming of thick-film electronic components and networks is a well-westablished and widely used technique in the hybride technology [16, 17]. Recently excimer laser induced ablation is applied in high feature density multi-chip module fabrication (MCM–C and MCM–D) for formation of holes and vias [18]. Since ablation is typically bound to a fluence threshold determined by the properties of both the thin film and the substrate, ablation was also used in laser beam profiling.

The material *removed* from the surface can be the subject of further applications. Since at high intensities (short laser pulses) the removed material, with respect to its atomic composition, is identical of the material of the surface, ablation offers an obvious possibility of chemical analysis of the surface by mass spectroscopy [19], laser microplasma analysis [20] etc. It should be noted that quantitative analysis by these methods is often suffered by matrix and resonance effects, non-equilibrium reordering of the material in the thermally affected zone, etc. However, comparative analysis at very low concentrations in environmental applications is demonstrated (e.g. [20]). Furthermore, the ablated material can be used as a source of atoms or ions, for e.g. measurement of plasma electron density [21] and silicon device doping, allowing the use of otherwise solid precursors for the process [22]. The non-thermal energy distribution of the material due to the non-equilibrium nature of the interaction of matter with high-intensity laser radiation is often used. Although not a thin film application, with regard to the continuously growing interest and year-by-year increasing number of publications, pulsed laser deposition (PLD, also denoted as laser ablation deposition, LAD) should also be mentioned (for a recent review outlining the main experimental facts and the numerous questions still open up to date, see Ref. [23]).

In the following I mention some important milestones of the development of the laser transfer technique.

Explosive bonding is a large-scale technique [24] which has been used extensively in industry to bond a thin layer of a more noble and costy metal to a heavier and less costy load-bearing substrate. In conventional *explosive bonding*, the thin layer of metal flyer plate to be bonded to the target substrate is impacted onto the substrate at high velocities via an explosive sheet charge. In 1983, Frish and Nebolsine demonstrated the possibility of explosive bonding of metal foils to substrates with pulsed laser beams [25]. The film thicknesses in these applications were a few tens of microns. Further improvement of this method was described by D. E. Alexander et al. by decreasing the thickness of the film down to one micron and scaling down the lateral dimensions to the millimeter range [26].

In our aspect the most important variant of the method is Laser-Induced Forward Transfer (LIFT) described by Bohandy et al. first in 1986 [27]. In LIFT a single metal layer is transferred from a transparent support onto the target surface (See Fig. 1). In the model proposed by the authors [27] the extensively heated material melts at the

support—film boundary first and then the melting front propagates throughout the thickness of the film. Finally a fraction of the layer facing the laser light evaporates, supplying thereby the propelling force necessary for the observed efficient transfer. By using this technique, deposition of an explosive layer prior to precoating the layer to be transferred is no more necessary. In addition, the future ability of this method of micrometer scale patterning could have been anticipated. (On the basis of the considerations described in Section 2.2., this appears to be no longer realistic.)

Of course, many interesting ideas arised from the LIFT technique. There were attempts to synthesize and transfer compound thin film patterns by single laser pulses, using a stack of elemental layer as donor film [28, 29, T1]. Pulsed laser-induced formation of metal patterns through pyrolysis of a metallo-organic film during laser transfer was described by Esrom et al [30] and direct writing by combined pyrolysis and transfer with cw lasers was also proposed [31]. Greer and coworkers applied laser-induced transfer of oxides for fine frequency trimming of surface acoustic wave resonator devices [32]. Doping of silicon with aluminium for solar application was performed by Toulemonde et al. by transferring the metal from a polymer substrate (Mylar) onto the silicon wafer with one ruby laser pulse and subsequent laser annealing [22]. Pulsed laser-induced transfer of thin film transistors, preformed on hydrogenated amorphous silicon film as substrate was planned by Sameshima et al. [33].

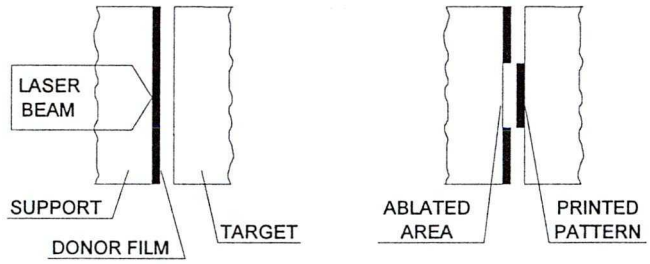

Fig. 1. Laser-Induced Forward Transfer (LIFT): a simple approach of deposition of thin film patterns. It should be noted that the use of the terms *donor/source* and *target* in this work is different from their interpretation in particle beam assisted technologies, where *target* usually denotes the object exposed to the radiation or beam emitted by the *source*. These terms are here used from the aspect of the material to be transferred: the original support is the source which holds the donor film to be transferred to the target.

1.2. Nanosecond-pulse induced LIFT

1.2.1. Introduction

Bohandy and coworkers did not give a convincing interpretation of the LIFT process. In later experiments the ablation and the transfer characteristics of thin metal films were found to be essentially not different when the film was irradiated through the support or the target substrate [34], which contradicts Bohandy's explanation. Although their picture may be appropriate for LIFT of thick films of materials with low heat conductivity illuminated through the glass support [35], the temperature disrtibution in thin metal films on thermally insulating substrate may exhibit larger inhomogeneities in *lateral* directions than across the film, unless the film thickness is definitely larger than the thermal diffusion length (see Ref. [36]).

Pulsed laser transfer experiments of the group lead by Tamás Szörényi in the Research Group on Laser Physics of the Hungarian Academy of Sciences, described in Ref. [34], have already shown that a range of different supported thin metal films exhibits

similar ablation and transfer characteristics as a function of processing laser fluence. In order to learn more about the nature of laser-induced transfer, a systematic experimental study has been launched using specially prepared thin films and an experimental arrangement which allowed variable distance between the source film and the substrate to be patterned [T2]. Correlation could be drawn between the support—film interface, the film-to-substrate distance and ablation and transfer yield.

1.2.2. Experimental arrangement

200 nm thick titanium films and 173 nm thick chromium films on glass substrates were used as donors to be transferred in the experiments. Two sets of standard microscope sample holder glass plates were differently prepared prior to electron beam evaporation of titanium: one set was cleaned by wet chemical methods only, while for the second set an additional cleaning step in glow discharge was applied. The adherence of the donor film to the support plate was controlled by the Scotch tape test. Titanium films deposited right after wet chemical cleaning could easily be removed indicating poor adherence, while glow discharge cleaning yielded well adhering films. The chrome samples (optical chrome masks) possessed excellent adherence.

The target substrates to be patterned were blank glass plates placed in an acute angle with the donor films, in direct contact along one edge. Thus, the distance between the surfaces varied between 0 and approx. 100 μm over the whole area (Fig. 2) and could be measured interferometrically at the position of processing ruby beam with an uncertainty below the wavelength of the measuring low-power He-Ne laser beam (λ=632.8 nm).

The processing Q-switched ruby laser supplied 20 ns long (FWHM, full width at half maximum) single pulses at $\lambda = 694$ nm, the pulse energy being approx. 800 mJ (Fig. 3). The laser pulse energy was monitored with a reference thermopile using a part of

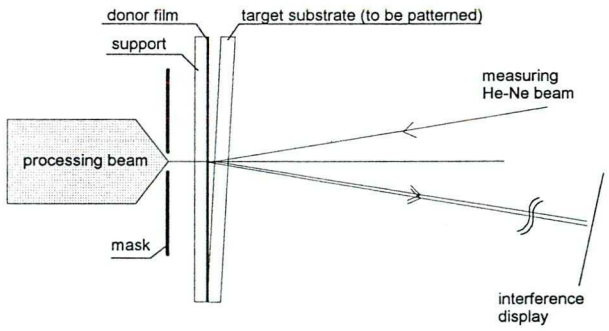

Fig. 2. Sample arrangement with variable donor—target distance in the LIFT experiments.

the laser output coupled out by a beam splitter. The laser beam was led through a set of attenuator plates and then collected into a homogenizer glass rod. Finally, the spatially homogeneous beam was shaped using a mask with a 1.8×1.8 mm^2 rectangular window. The source—target assembly was placed in contact with the mask. The laser energy density (from this point on: fluence) impinging the sample surface was tuned by the attenuators from 0 to above 1 J/cm^2, in steps of approx. 20 mJ/cm^2. Due to the errors in

the measurement of the laser pulse energy and the dimensions of the processed area, the overall uncertainty in the incident fluence values was estimated to be approx. 10%.

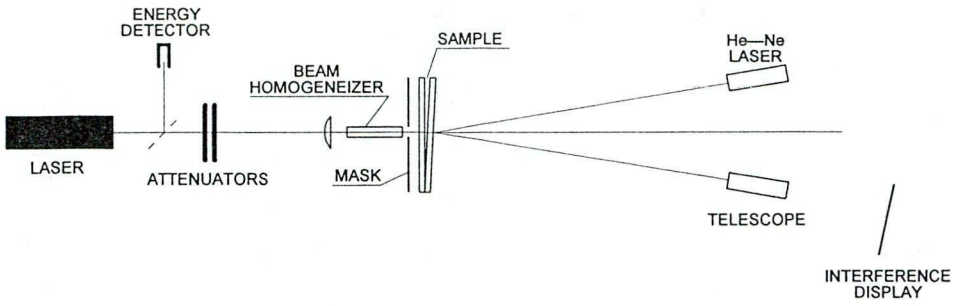

Fig. 3. LIFT experimental setup with controllable donor—target distance

The transfer efficiency was characterized with the transmittance of the central zone of the deposited patterns (prints) and the ablated areas by measuring the attenuation of a He-Ne laser beam (0.8 mm diameter, $\lambda = 632.8$ nm). For morphological characterization of both ablated and deposited areas, optical microscopy was applied.

1.2.3. Results

1.2.3.1. Laser transfer experiments

On performing the laser transfer with ns-pulses of high fluences (traditionally several J/cm^2, as usual in the ablation experiments), the high pressure developed from the partial evaporation of the film material propels the mixture of gas and molten particles from the support onto the target surface. Although 100% ablation efficiency can be obtained, the transferred material does not form a continuous layer on the surface to be patterned. The printed area consists of submicrometer spots formed by resolidified droplets and apparently condensed vapour. Even at minimum possible distances between the donor film and the target substrate, material spreads far beyond the contours of the laser spot, resulting in a considerable enlargement in print dimensions. Upon increasing the distance between the source and target surfaces from zero to approx. 100 μm, the width of the halo surrounding the illuminated area continuously extends from several tens of microns to even one millimeter. Parallelly, the transmittance of the central zone of the print pattern gradually increases (Fig. 4), which indicates decreasing transfer efficiency at longer distances. Debris formation and thermal damage of the target substrate further diminish the quality of the print patterns [T2]. Apparently, while smooth and well-covered "grey" prints could be produced with millimeter dimensions, such high-fluence processing does not give a way to produce micrometer-sized patterns of appropriate quality.

Since all these undesired features are consequences of the flash evaporation at high fluences, a logical step to avoid them is to decrease the processing fluence. When applying ns-pulses of fluences which are sufficient for melting the film material only, the ablation efficiency strongly decreases (Fig. 5), a substantial amount of the film material remains on the original substrate in the form of resolidified droplets. Although the removed molten particles adhere fairly well to the substrate to be patterned, they form a non-contiguous print pattern with little control over the lateral dimensions [T1,T2]. In this fluence range there is no apparent correspondence between the ablation and transfer efficiency and donor—target distances below 80 μm (Fig. 4).

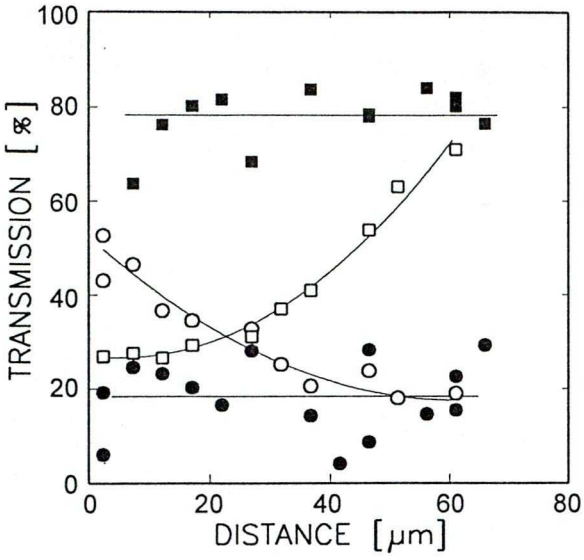

Fig. 4. Transmittance of the ablated areas (circles) and print patterns (squares) for the chromium sample, measured at the He-Ne laser wavelength for high and intermediate fluences (900±50 mJ/cm^2—open symbols, 375±25 mJ/cm^2—full symbols, respectively). In these fluence ranges the film temperatures are typical of evaporation and melting, respectively.

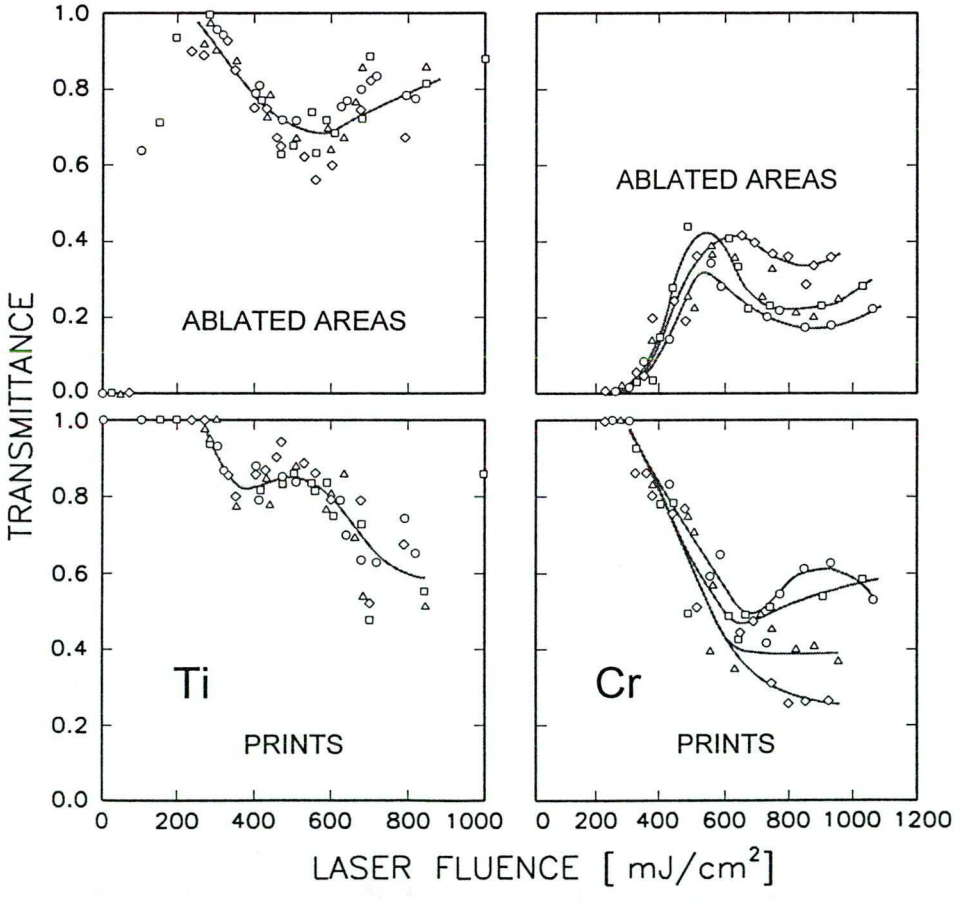

Fig. 5. Measured transmittance of the ablated areas and the corresponding prints of poorly adhering Ti films (left panel) and well adhering chromium films (right panel), respectively, as a function of the incident laser fluence. The spacing between the donor film and the substrate is 15 (◇), 35 (△), 45 (□) and 55 μm (○), respectively.

Upon further decreasing the fluence, a process window exists which offers a completely different and novel approach to thin film ablation and transfer (Fig. 5). Our systematic studies revealed that, unlike the case of ablation of bulk materials, where evaporation is the only possibility of thermal ablation, single laser pulses of rather low fluence could completely remove thin films over the whole irradiated area in the solid phase, without any damage of the underlying substrate (*clean ablation*). Unfortunately, when using nanosecond-pulses, this highly efficient removal was not accompanied by efficient deposition of the removed material. Adhesion of the transferred pattern was rather poor since the landing (metal) piece did not have enough energy to establish firm adherence to the surface to be patterned. [T2, T1].

The above described disadvantages of ablation and transfer with conventional high-fluence pulses were already mentioned also by other authors [27, 34, 37, 38, 39]. However, the clean ablation phenomenon had no reference in the literature. This is due to the fact that ablation was conventionally performed using high fluence laser pulses, 1 J/cm^2 and above, which are sufficient for evaporation of the material. Only a few publications dealt with the application of lower fluences, mainly to determine the ablation or damage threshold [39, 40, 41, 42, 43, 44].

The conclusion of this study is that ns-pulse processing is difficult to optimize for micrometer resolution pattern production. Using high fluences, resulting in melting or evaporation of the film material, the quality and dimensions of the deposited pattern can not be properly controlled.

1.2.3.2. Clean ablation of thin metal films

Nanosecond-pulse induced clean ablation of thin films due to pure mechanical effects was observed for most investigated metal—substrate pairs (V, Sn [34], Ti [T1], Cu [45], W [45, 46, 47, T3, T4]), some non-metallic films (Ge [28, 45, T1]), the substrates being glass or quartz, but not for some extremely well-adhering layers, e.g. optical chrome masks [39, T2, T1]. The fluence window for clean ablation was found to extend from 60 to 300 mJ/cm^2 for 68 nm thick vanadium, from 100 to 200 mJ/cm^2 for 200 nm thick titanium and from 40 to 200 mJ/cm^2 for 100 nm thick tungsten films, respectively. Differences in the reflectivity, thermophysical and mechanical properties and in the preparation may account for the differences in the characteristic fluence values. In all cases, the thin films were removed from the total illuminated area, while the underlying substrates remained always intact. The edges of the ablated areas and those of the metal chips occasionally remaining on the original substrate surface were of abrupt contours without any traces of melting suggesting that ablation commenced with ripping off of the solid metal film.

Numerical calculation of the temperatures was performed for each set of processing parameters used in the experiments. Since the lateral dimensions of the processed areas were large as compared to the thermal diffusion lengths, the one-dimensional model was used, supposing tight thermal contact between the thin film and its substrate. The calculated maximum temperatures within the thin films were always below the melting point, which also proved that clean ablation of the metal films took place in the solid phase.

Pictures of the flying ablated pieces of a 100 nm thick tungsten film gave independent experimental evidence that the material left the substrate surface in form of solid pieces (Fig. 6) [T3, T4]. These pictures were taken by ultrafast photography using

1 ns long recording pulses from a N_2 laser pumped dye laser delayed by 0.1-200 μs after the ablating ArF excimer laser pulse.

As revealed by time-resolved transmittance and reflectivity data [47], as well as nanosecond-resolution photographic imaging [T3, T4], the ablated solid pieces can travel distances of millimeters even in air, however, subsequent to ablation they lose most of their kinetic energy and begin uncontrollable rotation. Further energy is lost due to radiative and convective cooling. In laser transfer configuration, upon impact, the remainder thermal energy diffuses promptly into the target substrate without heating it up to its softening temperature. Thus, the highly efficient removal is not accompanied with efficient deposition of the removed material because of the poor adherence of the deposits [34, T1, T2].

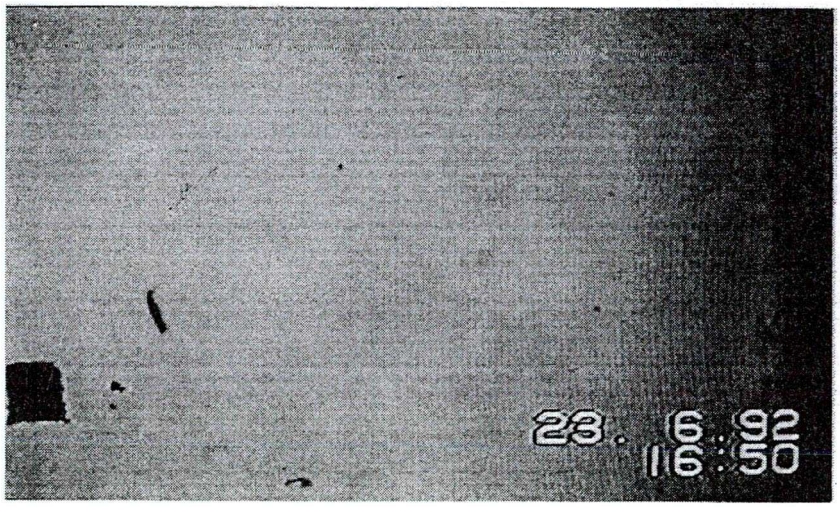

Fig. 6. 0.5×0.6 mm large, 100 nm thick tungsten pattern after ablation from a soda lime glass substrate (left edge) in atmospheric air. The delay time of the photographic dye laser pulse (1 nm FWHM) after the processing ArF excimer laser pulse was 390 μs, the distance between the substrate and the pattern being approx. 4.5 mm.

The mechanism of the clean ablation is not satisfactorily described yet. Chromium and gold did not show clean ablation at all [39, 40, 48, T1, T2], while, as shown above, in the case of titanium, the interface properties played selective role in clean ablation. Thin vanadium films were reported to possess always clean ablation behaviour, with slight variation in the ablation threshold fluence with different substrate preparation methods prior to deposition of the donor film [34]. We propose the following picture: in this clean ablation window, because of the critical difference in the mechanical properties of the metal film and the glass support, the elevated temperatures lead to the rise of elastic tensions at the metal—glass interface exceeding adhesion. Propelling forces which arise from evaporation of local contaminations at the metal-substrate interface can also contribute to film removal [34, T1, T2, T3, T4, T5, T6].

Since metals are good heat conductors (more specifically, the thermal diffusion length — for pulse durations in the order of tens of nanoseconds — is typically in the order of micrometers), metal films of several hundred nm thicknesses are homogeneously and instantaneously heated in their total depth. An immediate consequence of this homogeneous heating is an uniform response of the total metal layer. For example, upon processing with fluences which are sufficient to melt the material, such metal films start to melt at tiny seeds locally, due to the lateral inhomogeneities, leaving small separated holes, rather than melting through layer-by-layer from the irradiated surface to the other

boundary uniformly over the processed area [36, 49, 50, 51, T1, T3, T4]. This effect may account for the observed drastical decrease of the ablation efficiency upon melting the material, as compared to the 100% removal by clean ablation, since elastic forces are cancelled with the formation of liquid phase and the encapsulated gases can escape via interdroplet spaces.

Even though efficient deposition of the patterns ablated with nanosecond-pulses proved to be impossible, solid-phase clean ablation still offers the possibility of micrometer-resolution patterning of surfaces. Clearly, further optimization is necessary to define process parameter ranges in which not only the good morphology of the ablated pattern can be preserved, but firm adherence to the surface to be patterned can also be ensured. In other words: a way has to be found to transfer sufficient energy for the firm adherence of the solid landing pattern.

Since melting sets the upper limit of the clean ablation, any increase in the temperature of the landing piece can only be realized when transferring a material of (relatively) high melting point. The power and duration of the processing pulse should be tuned to produce clean ablation and maintain sufficient temperature during film transfer and impact, to ensure heat transfer from the landing piece to the substrate to be patterned for good adherence.

1.3. Long-pulse laser transfer

1.3.1. Introduction

The above analysis of laser transfer experiments with *nanosecond-pulses* revealed that micrometer-resolution patterning could be realized more probably with longer pulses, however, could not give any closer approximation to the optimal time scale of the processing. In this section results of our experimental studies on long-pulse laser transfer are presented. First, the laser microprocessing and monitoring system, based on a diode-pumped Nd:YAG laser, which allows generation of laser pulses of arbitrary time course, duration and peak power, and is, thereby, the simplest and most elegant tool for the optimization of the laser pulse parameters will be described. It will be shown that well adhering micrometer sized patterns of 100% coverage preserving the shape and dimensions of the ablated area can be deposited by ablating and transferring tungsten thin films in form of single solid pieces using single pulses of peak power up to 100 mW and 100 μs - 1 ms duration. Then the analysis of the time evolution of the process will be presented, as followed by real-time measurements of the reflectivity and transmittance of the illuminated film areas during processing.

1.3.2. The microsecond-pulse laser micromachining and monitoring system

The scheme of the experimental setup which played a basic role in my experiments in long laser pulse-induced transfer of thin metal films (Section 2.3.) and laser-induced synthesis of ZnSe compound semiconductor films (Section 3.) is shown in Fig. 7. The details of operation are given below.

Laser and control system. Extended modulation bandwidth.

The laser used in the experiments was a DPY 321 model (ADLAS) diode-pumped Nd:YAG laser emitting single TEM_{00} mode beam at 1064 nm wavelength in the near infrared, the beam diameter and divergency {at the laser output} being 1.0 mm and <1.8 mrad, respectively. The maximum continuous wave (cw) laser power is 750 mW.

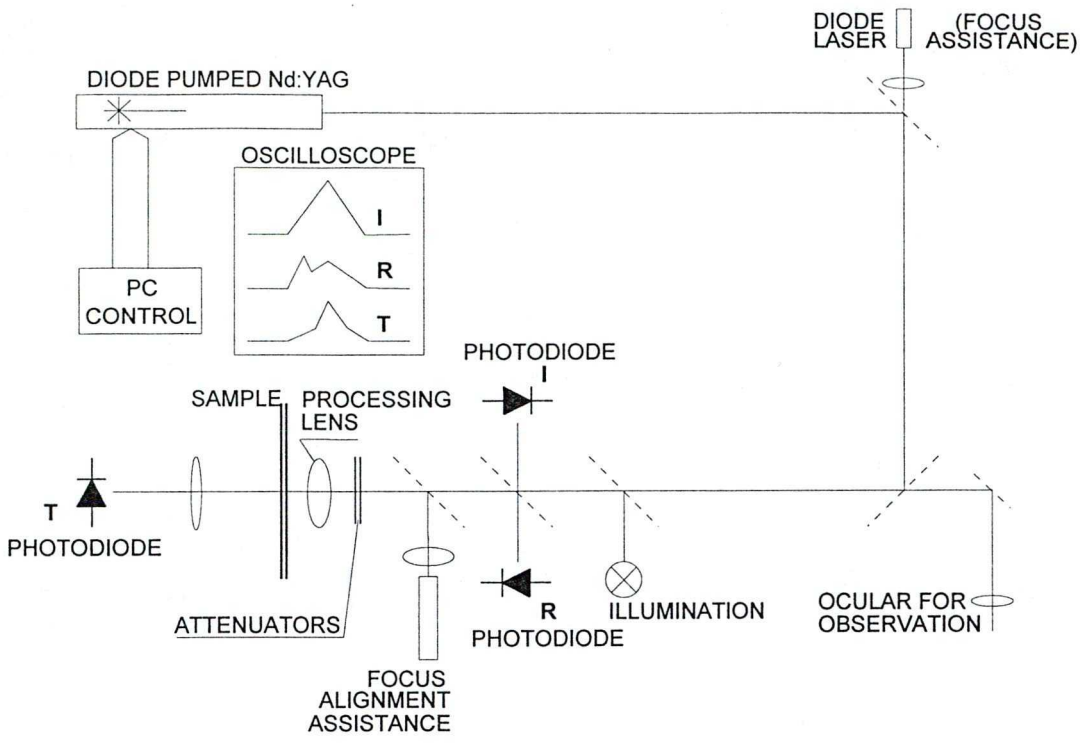

Fig. 7. Schematic diagram of the long-pulse laser microprocessing and monitoring system.

The factory-supplied electronic control unit allows external control of the pumping diode lasers accepting arbitrary input signal between 0 and 5 VDC. Until the control voltage is constant or its modulation bandwidth doesn't exceed a critical value (approx. 1 kHz [52]), the diode laser output and, therefore, the YAG output are linear functions of the control voltage above their respective, well defined operation thresholds (Fig. 8). When the critical modulation bandwidth is exceeded, (e.g. when the rise time of the control signal from zero to maximum becomes shorter than approx. 1 ms), the YAG output exhibits a spiking behaviour as typical of solid state lasers. Spiking laser output corresponding to an abrupt control signal rising from 0 to 3.1 V is shown in Fig. 9, as appeared on the oscilloscope display.

In order to avoid this undesired feature and to expand the modulation bandwidth, or in other words, to decrease the allowable rise times and pulse widths, the control signal was kept above the operation threshold of YAG, i.e. the population inversion was continuously maintained. Naturally, this operation mode was accompanied with the presence of a cw background power of approx. 3-7 mW at the laser output (for shorter rise times the higher value must be set). In certain applications this background may be harmful when low processing peak powers are required, thus, the laser was always controlled with large modulation depth between approx. 65 and 100%, and before the focusing microscope objective a set of gray attenuator plates of 65 to 70% transmittance (for each, at 1064 nm) was inserted (Fig. 7) for the suppression of the background radiation. For demonstration of the possibilities of this operation mode, oscilloscope traces of triangle shape laser pulses are shown in Fig. 10. (b).

In the experiments the laser control signal was produced by either an analogue signal generator [T6, T5], or a computer-driven eight-bit D/A converter [T7, T8]. In this latter case, within the limits of the extended modulation bandwidth, arbitrary laser pulses could easily be defined, simply by sending a series of 8-bit data referring to the desired

intensity as a function of time with 1 μs time resolution through the D/A converter card to the laser control input socket.

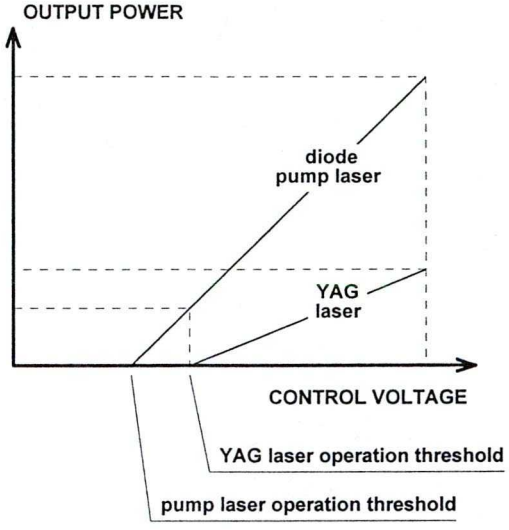

Fig. 8. Relationship between control voltage of the laser power supply, output of the diode laser and output of the YAG laser.

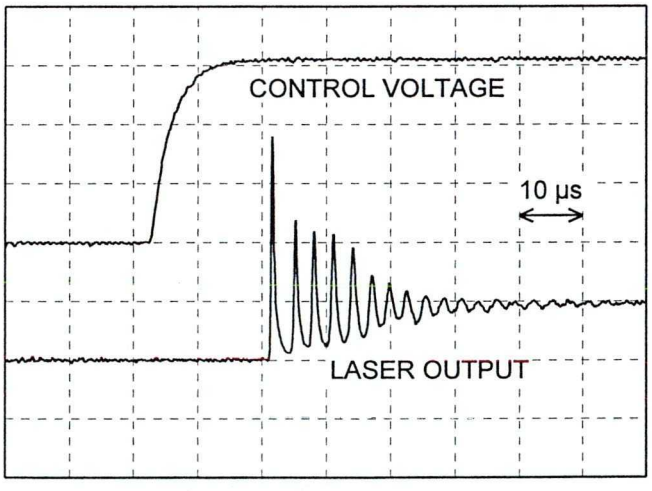

Fig. 9. Copy of the oscilloscope display showing spiking laser output corresponding to an abrupt control signal rising from 0 to 3.1 V. The horizontal scale is 10 μs/div, the control voltage is drawn with 1 V/div scaling, while the laser intensity can be read in a.u. (Note that the shape of the ~500 ns wide spike profiles are distorted because of the finite temporal resolution of the measurement.)

Beam delivery

After the laser output window, the laser beam was reflected twice by dielectric mirrors in 45° incidence (Fig. 7). The dielectric mirrors were of high reflection (>99%) at the processing wavelength and in the visible they served as beam splitters. The laser beam was then led through beam splitters (see below) and the grey attenuators aiding the optimum control of the laser and finally through the focusing element. Focus diameters

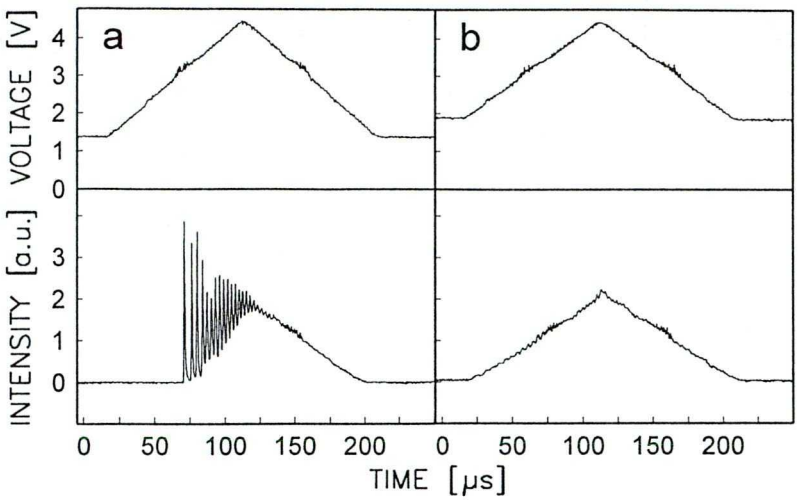

Fig. 10. Spiking behaviour (a) and regular operation (b) of the diode-pumped Nd:YAG laser. The time course of the external control signal and the corresponding laser output are shown as top and bottom curves in each panel, respectively. The triangle shape control signal is settled onto a DC level of 1.42 and 1.92 V for (a) and (b), respectively. The control voltage threshold for stable continuous operation is at approx. 1.8 V.

down to few microns have been achieved by focusing the infrared beam with microscope objectives (e.g. with a 20×/0.35 Zeiss objective the measured diameter of the focal spot was 6.3 μm , close to the diffraction-limited value of approx. 3.9 μm). The focus diameter was measured by the so-called scanning knife edge method.

Focus alignment and sample motion

Before each pulse the focus was finely realigned by translating the sample holder along the axis parallel to the beam propagation. For the detection of the right position of the sample, a red diode laser was coupled into the beam path through the first dielectric mirror, coaxially with the YAG beam. After reflection from the sample, the beam of the diode laser was coupled out by a beam splitter and observed through a focusing microscope. The sample was moved in-plane by step motors with 5 μm resolution, which was also controlled by the computer.

Photodiodes

After the second mirror, a beam splitter was inserted to deliver a part of the processing light onto the sensitive area of a reference photodiode **I** (laser "intensity"; see Fig. 7). A part of the light reflected from the processed sample surface propagating backwards in the beam path was projected onto photodiode **R** ("reflection"). The main part of the processing light passing through the illuminated sample was collected by a lens onto the third photodiode **T** ("transmission"). The three photodiode heads with built-in preamplifiers converted the incident light intensity into voltage with a transmission bandwidth of approx. 0.5 MHz. The photodiode signals were measured by a digitizing oscilloscope (PHILIPS PM97 [T7, T9] or HAMEG HM 205-3 [T8]) and then loaded into the computer for numerical evaluation. The same computer was used to control the laser, to process the measured real-time optical data and to control the translation of the sample, providing, thereby, a rather convenient research environment.

1.3.3. Experimental details

The experimental work was carried out in two phases. In the first, we demonstrated the feasibility of the long-pulse laser transfer method. In the second phase the dynamics of the process was examined.

In the first series of experiments tungsten films of 200 nm thickness deposited onto glass substrates by electron beam evaporation were used as the material to be transferred. Substrates to be patterned were glass plates fixed vertically in contact with the tungsten films with a pressure of several kPa-s. The films were illuminated through the support with the focused Gaussian beam (TEM_{00}) of the diode-pumped YAG laser. The shape of the processing laser pulse was controlled by an analogue signal generator and the full width at half maximum (FWHM) of the triangular pulses was varied between 100 μs and 1 ms, the peak power being adjusted between 0 and 200 mW. The $1/e^2$ diameter of the processing laser spot was 9 μm.

The time course of the process was followed on 100 nm thick tungsten film samples. The substrates to be patterned were glass microscope slides facing the metal film at distances well below 1 μm as measured interferometrically. The donor—target assembly was processed in the above described laser microprocessing and monitoring system. The metal film was irradiated through its support with focused laser beam. The single processing pulses were of symmetric triangle shape of 100, 500 or 1000 μs half widths and 20 to 240 mW peak powers at the film-support interface. The $1/e^2$ diameter of the focal spot was 8.1 μm. The microsecond-pulse laser micromachining and monitoring system allowed us to follow the evolution of both the reflection and transmittance of the processed thin film area during processing. Since the probe beam was the Gaussian processing beam itself, the dominant piece of information was derived from the central part of the illuminated area. Because of the finite aperture of the collecting lens and the measuring diode heads, the system was sensitive to the geometrical changes of the film surface (bending, translation etc.) indicated by changes in reflection, not necessarily accompanied with concomitant changes in the transmitted signal. Since the transmittance of the untreated tungsten layer is low compared to the reflectivity (< 1% and 28%, respectively, measured at λ=1.064 μm, the wavelength of the processing laser) relatively large changes of its absolute values may cause no apparent changes in the reflection signal. A decrease in reflection accompanied with simultaneous increase in transmission is a clear indication of the onset of ablation.

The ablated areas and the deposited prints were characterized by optical microscopy; high resolution images were obtained by scanning electron microscopy (SEM) in secondary (SEI) and backscattered electron imaging (BEI) mode. In this latter case a low angle detector was used for recording the 3D local topography.

1.3.4. Results

When processing with pulses of 100 μs FWHM, the onset of ablation and print formation commences at 50-55 mW peak power. As revealed by SEM images (not shown) the tungsten film is partially peeled off along a circle of 6-7 μm diameter. The ablated metal fragments are detected both on the support and the print faces indicating that the adherence onto the substrate to be patterned is incomplete. On increasing the power the probability of successful printing is increasing. Pulses of 70-110 mW peak power result in significantly more minute (3-4 μm dimensions) well adhering print patterns of rather irregular contours. These prints are transferred from the central parts of the (deformed) processed film areas.

At 110 mW the metal film is completely separated along the whole circumference of the illuminated area. As seen in the SEM micrographs, the ablated area and the transferred pattern perfectly match, indicating that the film has been ablated and transferred in form of a single solid piece. The backscattered electron image of the print pattern convincingly demonstrates that the deposit uniformly adheres to the substrate practically on its whole surface. The best quality printing is observed in a narrow power window, the upper limit being at approx. 120 mW. In the central area of the deposits several miniature cracks appear as dark lines in the secondary electron image probably due to elastic stresses arising in the hot metal piece when being cooled down after the end of the illumination.

Exceeding this power the metal film in the central part of the processed area is deteriorated and is usually observed on the support, while the surrounding metal rim forms a ring-shaped print. It is important to note that no traces of melting can be seen on the metal structures, even in the central region. The glass substrate, on the other hand, is obviously damaged due to the local thermal load in the place in contact with the central tungsten part; the originally even surface of the glass substrate becomes rough and exhibits irregular protrusions. Similar damaged areas are observed in the central parts of the SEM micrographs of the glass support.

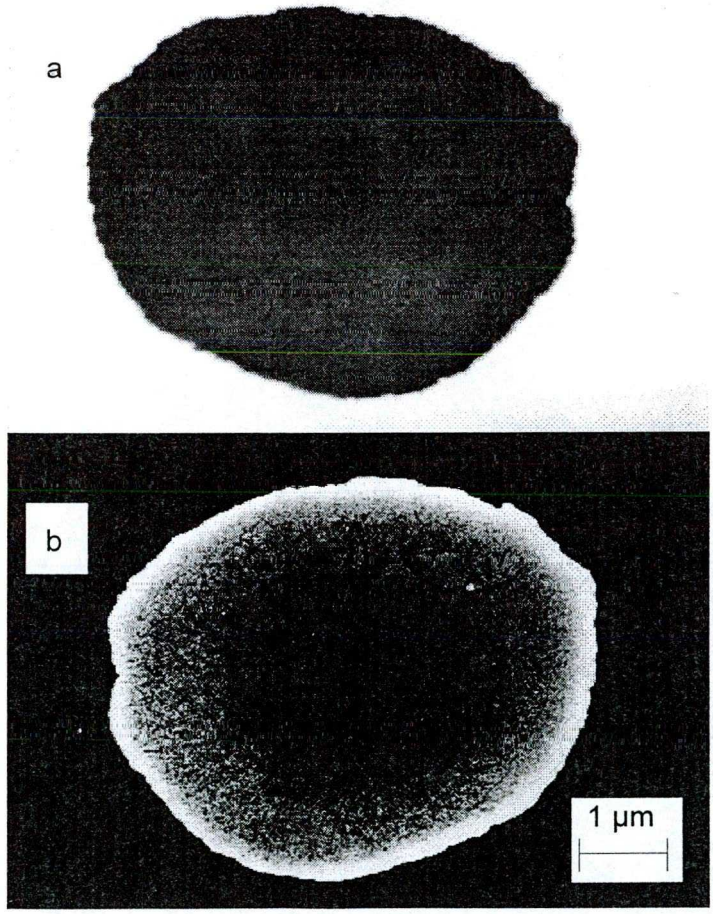

Fig. 11. Backscattered electron images of the ablated area (a) and the corresponding print (b). The peak power and the FWHM of the pulse were 65 mW and 1 ms, respectively. The scaling bar indicates 1 µm. Typical undulations of the deposited surface pattern are in the order of tenths of a micron. The good adherence of the patterns is proved with Scotch-tape test.

With increasing pulse duration this sequence of events remains unaltered although becomes more gradual; the appropriate thresholds are shifted towards lower powers. Using pulses of 1 ms FWHM the onset of print formation is observed at 35-40 mW, but unlike in the case of 100 μs pulses, closely above this threshold well adhering continuous print patterns of ≈6 μm diameter are deposited. The ideal power range for processing, which is between 110 and 120 mW using 100 μs pulses, is now observed between 60 and 70 mW. As shown in Fig. 11, the ablated area and the corresponding print pattern precisely match and the well adhering deposit has 100% coverage. Contrary to the patterns produced with 100 μs pulses, however, there is no sign of thermal load on either the ablated area or the print. Exceeding 70 mW the central area becomes gradually thinner and damaged as described above; with further increase in power the ring structure dominates.

1.3.5. Discussion

Optical microscopic and SEM observations of the transferred patterns and the surface of the donor substrate did not reveal any traces of melting.

Temperature profile calculations also strengthened this observation. The thermal conductivity equation was solved numerically using the method of finite differences [53] (see Appendix). The temperature dependence of thermophysical parameters was taken into account. Resulting from the temperature, there is a very little change in the optical properties of tungsten, thus the reflectivity was assumed to be constant. From the point of view of heat exchange, the process can be modelled by assuming steady thermal contact between the metal film and the support prior to ablation and after landing, or free standing metal during the transfer. The temperature values plotted in Fig. 12 have been calculated in the frame of this latter approximation, i.e. assuming no thermal contact between the metal film and the support. Obviously, this approximation results in calculated temperatures definitely higher than those appearing in the real system, where significant heat conduction toward the substrate is apparent. Nevertheless, up to 135 mW even these overestimated temperature values remain below the melting point of tungsten, T_m=3653 K. This is consistent with the observation that ablation starts in solid phase in the whole power regime investigated. After landing, heat diffusion from the solid metal piece to the glass substrate (to be patterned) is controlled by the laser intensity and duration of the processing pulse allowing fine tuning of substrate temperature and thereby the adherence of the pattern.

When ablating with pulses of 100 μs FWHM and ≈60 mW peak power even the maximum temperature of the metal is only slightly above 1000 K (Fig. 12) and the heating of the glass substrate has relatively short duration (certainly much less than 100 μs). In this instance the glass material hardly reaches its softening temperature even in the centre of the processed area and consequently the metal piece does not adhere to the "cold" glass surface. On increasing the peak power to 117 mW the model calculations predict maximum metal temperatures at around 2000 K over a central area of 5 μm diameter (Fig. 12). Heat transfer from the landing hot metal layer to the substrate will bring about temporary heating of a few-micrometer thick layer of the glass up to its softening temperature (≈1000 K) ensuring excellent adherence over the whole metal-glass interface. Further increase in processing power represents a massive thermal overload in the glass substrate which ultimately leads to strong deformation. The central area of both the original support (to lesser extent) and the substrate to be patterned (to larger extent) is doomed and the glass faces damage the central part of the metal pattern.

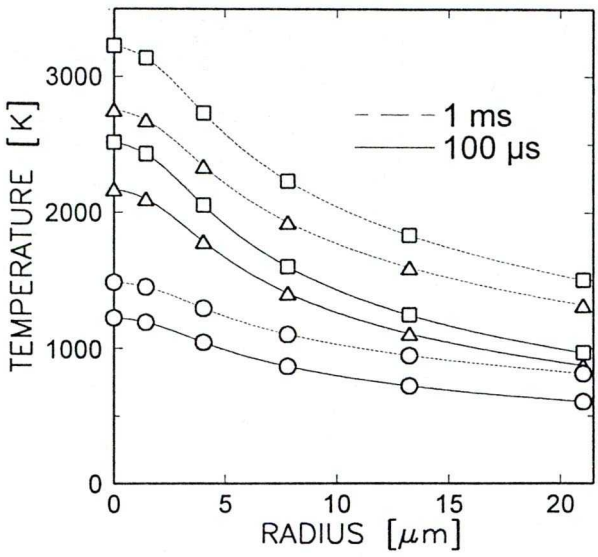

Fig. 12. Lateral distribution of the calculated temperatures (see in text) of a free standing tungsten film of 200 nm thickness at the instant, as the film temperature reaches its maximum value in the centre. The processing pulses are of triangular shape with 100 μs and 1 ms FWHM (solid and dashed lines, respectively) . The beam diameter is 9 μm. Peak powers: (O) 64 mW; (Δ) 117 mW; ( ) 135 mW.

The increase of FWHM of the processing pulses has the obvious advantage that durable heat diffusion ensures more complete on-site annealing since the pulse duration is significantly longer than the time needed for ablation. After sufficiently long time the softened glass texture can match the replica surface of the transferred solid tungsten film more effectively creating thereby stronger adhesive contact. In addition, longer pulses result in somewhat higher temperatures (c.f. Fig. 12). Consequently, using pulses of 1 ms FWHM, the process window for appropriate print pattern formation is broadened and its power limit is shifted to lower values. It should be added that variation of FWHM provides, from the technological point of view, a rather convenient means for fine control of the process.

In summary, the above experiments demonstrated the possibility of long laser pulse-induced transfer of μm-sized thin metal patterns in solid phase. However, important questions remained essentially unanswered yet. What is the fundamental mechanism of this long-pulse laser transfer? What is the influence of the pulse parameters on removal and transfer? How is good adhesion of the transferred pattern achieved? Further experiments, enlightening the dynamics of the process have been addressed to these issues.

1.4. Long-pulse laser transfer: the time evolution of the process as followed by real-time measurement of reflectivity and transmittance

1.4.1. Introduction

In section 2.3. the feasibility of transferring tungsten patterns onto substrates in direct contact with the donor film using long laser pulses. [28, T5, T6] has been demonstrated. However, during this study it was recognized that deeper understanding of the time evolution of the process was necessary for further optimization of the long-pulse solid-phase laser transfer process. For this aim, real-time measurements of the

transmittance and reflectivity of the illuminated areas during laser processing were performed.

1.4.2. Results and discussion

1.4.2.1. Real-time reflection and transmission measurements

Depending on the peak power, the recorded transmission and reflection curves displayed characteristic deviations from the triangle shape of the incident processing pulse regardless of the duration of the incident pulse. Since the optical absorption has negligible temperature dependence, the deviations in the recorded time-dependent curves are indicative of geometrical changes associated with donor film bending, in-plane fracturing, non-uniform removal from the support face and melting, etc. Since the highest temperature occurs always in the centre of the irradiated spot, the temperature-driven processes initially take place in the middle of the structure. Thus, in analyzing the time-dependent reflectivity and transmission curves (Fig. 13, a—h) it is assumed that the onset of the characteristic changes in the recorded optical signals refers to the start of the processes at the centre, while their duration is interpreted as the time needed for the completion of a given process over the total illuminated area.

Four characteristic types of features are apparent in the reflection and transmission curves, as illustrated by the example of 500 μs FWHM pulse processing in Fig. 13. At low power (20 to 90 mW) the transmitted signal was linearly proportional to the processing incident intensity until a well-defined point in the first half of the processing pulse (Fig. 13, a and b); after this point slightly decreasing slope was observed. As the processing peak power was increased, this characteristic breakpoint could be detected earlier in the transmitted signal. No corresponding feature was observed in the reflection signal indicating that the metal film remained continuous. On increasing the peak power to 40 mW, as a second feature, a sudden increase of the reflection signal was observed during the first half of the processing pulse, while the trend of the transmission signal remained unchanged (Fig. 13, b—d). For incident powers below 100 mW, the reflection curve increased approximately linearly until the peak of the processing pulse.

For pulses with peak powers exceeding 100 mW a new feature was observed in addition to the characteristics described above. From a given time-point the steep increase in the reflection curve continued with a sudden decrease (Fig. 13, e—h). Corresponding to this decreased reflectivity, the transmission signal possessed a simultaneous increase. These simultaneous changes which indicate the damage of the integrity of the layer (probably upon ablation and transfer) lasted approx. 150-300 μs; this time can be treated as the time necessary for the completion of the processes resulting in this third feature of the optical signals. After the completion of these changes both the reflection and the transmission signals became proportional to the processing laser intensity. Similarly to the first one, the second and the third features appeared progressively earlier when the processing peak power was increased. (On shortening the pulse width from 500 to 100 μs this third feature was detected above 120 mW processing power.)

On further increasing the processing laser power, above 150 mW the reflection *vs.* time curve showed an additional feature at the end of the falling period of the processing pulse (Fig. 13, f—h). The reflection signal temporarily increased, while the transmission signal decreased. The fourth feature was not detected for 100 μs pulse width, while it was more pronounced in the curves recorded during processing with 1000 μs wide pulses.

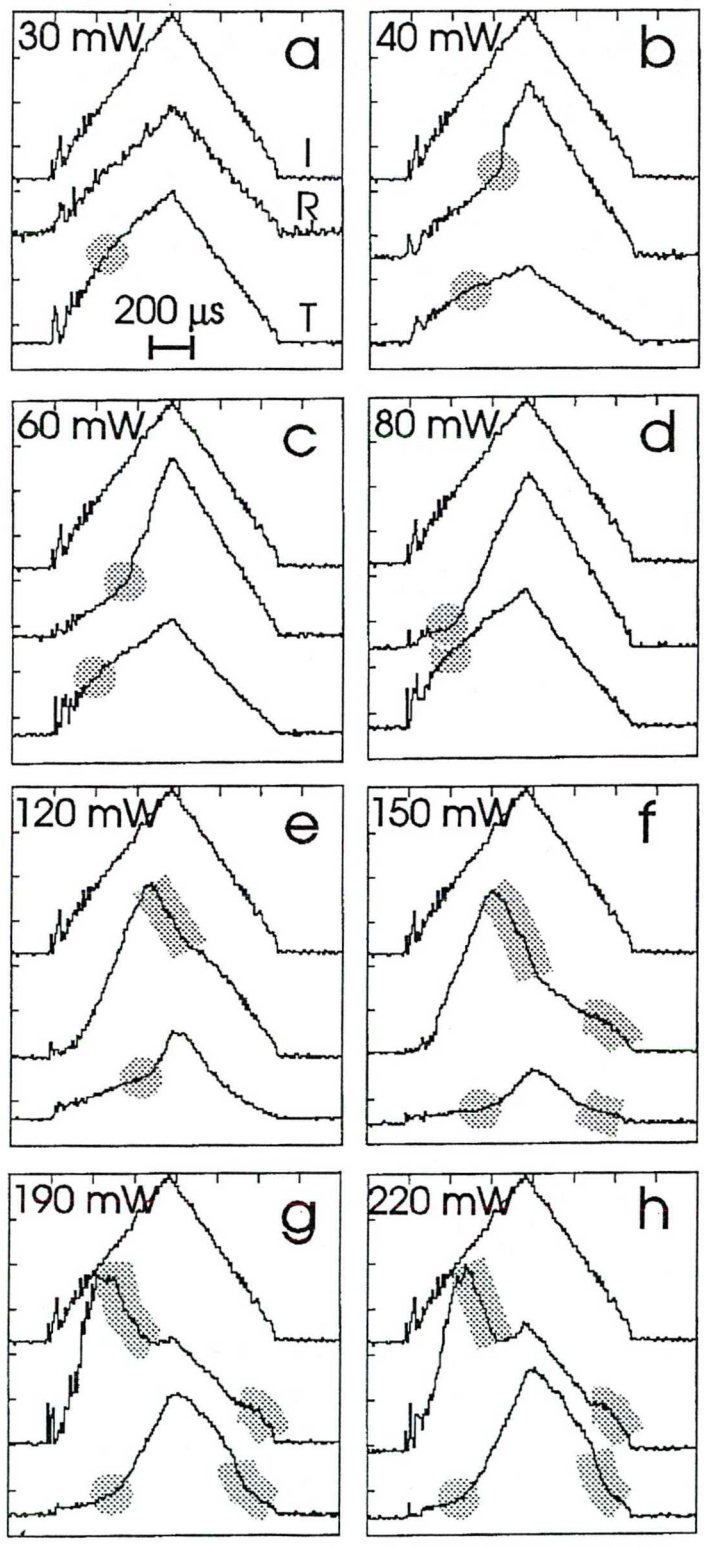

Fig. 13. Time-resolved curves of the optical properties of the processed area using 500 µs wide (at half maximum) processing pulses with 30, 40, 60, 80, 120, 150, 190 and 220 mW peak powers (a to h, respectively). The top curve in each panel is the intensity of the processing pulse, the middle and bottom curves are the reflectivity and the transmission, respectively. The four apparent characteristic features of the curves are marked with shaded symbols. The unit on the horizontal axis is 200 µs. The vertical scale, intensity is drawn with arbitrary units.

For the first three features essentially the same trends were observed using shorter and longer processing pulses of 100 and 1000 μs full width at half maximum, respectively, but unlike the 500 μs case, the process causing the third feature (parallel decrease and increase of the reflection and transmission signals, respectively) was apparently incomplete within the duration of the 100 μs pulses, even in the high peak power domain.

1.4.2.2. Morphological characterization of the ablated areas and the deposited patterns

Optical and scanning electron microscopic characterization of the processed areas revealed that 500 μs long pulses with peak powers between 20 and 90 mW did not result in ablation. High resolution backscattered electron images of the processed donor film (Fig. 14) clearly showed that the tungsten layer remained continuous, but was deformed with bulges whose diameters increased with increasing peak power up to approx. 9 μm.

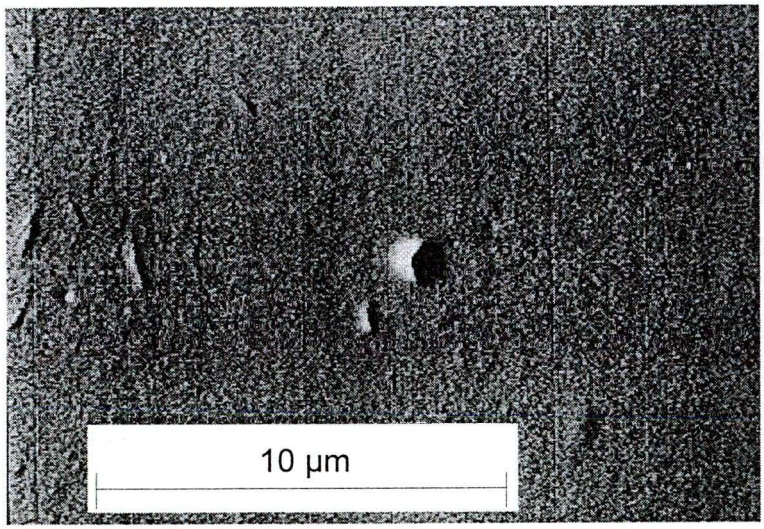

Fig. 14. Backscattered electron image of the deformation of the donor film produced by low-power irradiation with a 500 μs long laser pulse at 20 mW.

Processing with peak powers between 100 and 140 mW resulted in ablation and deposition of the ablated pattern in the form of single pieces. Fig. 15a shows a scanning electron micrograph of 100 nm thick, well adhering tungsten patterns deposited onto glass substrate with 500 μs wide triangular pulses and a peak power of 130 mW. The lateral dimensions of the deposited patterns matched those of the processing laser spot within ±2 microns. As being transferred in the solid phase, the film thickness did not change during transfer. Typical unevenness of the deposited surface patterns is in the order of tenths of a micron.

An increase in the peak power caused the film in the central part of the print patterns to be strongly distorted (Fig. 15b). A certain amount of tungsten remained in the middle of the ablated area, forming a small ring at the lower powers (≤160 mW), while at higher powers (>160 mW) structureless debris was observed. Above 180 mW peak power print patterns with fragmented edges and central zones were deposited.

The same trend was observed for processing with 1000 μs long pulses, with slightly lower values of the characteristic peak powers. Ablation and concomitant deposition of the single metal pieces with contours matching the processing laser spot were observed above 100 mW, first in a random manner and then systematically for slightly higher powers. Above 130 mW the central part of the ablated holes was coated

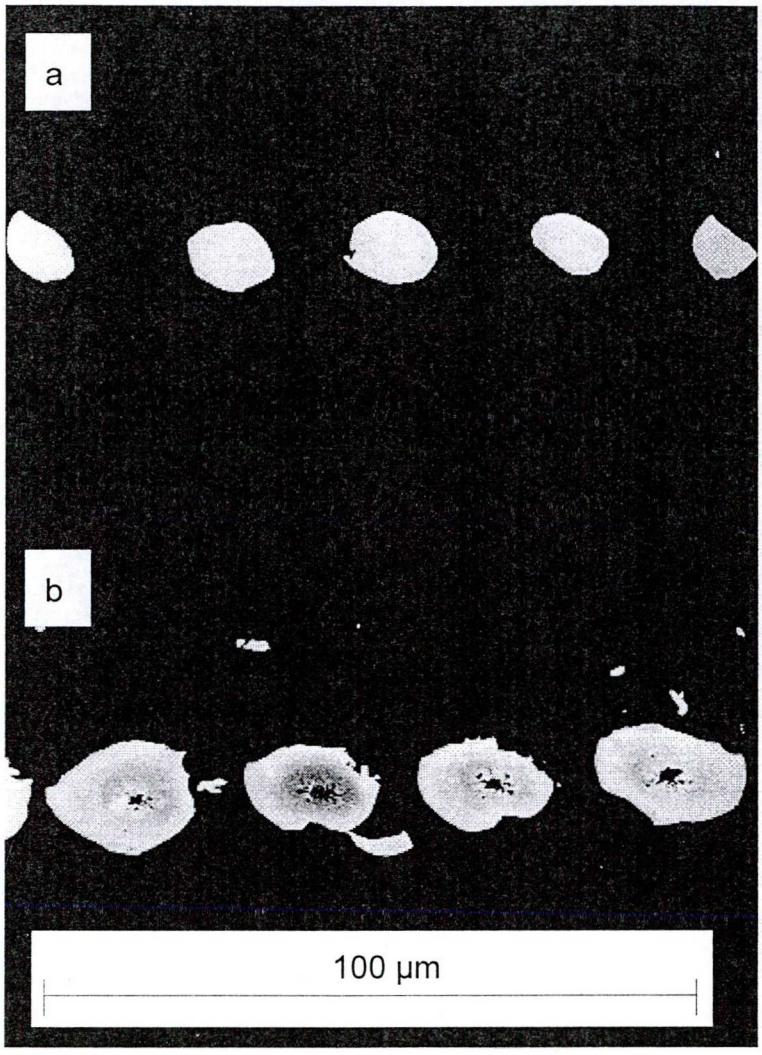

Fig. 15. Electron microscopic images of print patterns produced with 500 µs long laser pulses of (a) 130 mW and (b) 200 mW peak powers (backscattered and secondary electron images, respectively). Typical undulations of the deposited surface patterns (a) are in the order of tenths of a micron. The good adherence of these patterns was proven with Scotch-tape test and in ultrasound bath. The peripheral parts of the patterns (b) could be teared off by the adhesive tape.

with tungsten, which was ordered first into a small ring and then, on increasing the peak power, it became structureless with gradually decreasing amount. Above 170 mW the ablated holes were clear again with ragged edges; the edges of the print patterns were also damaged.

The ablation threshold for 100 µs long pulses was found at approx. 120 mW peak power. Pulses above this value resulted in complete ablation and deposition of print patterns with ragged edges indicating incomplete adherence at the edges of the patterns. Increasing the peak power above 160 mW led to the thermal damage of the central part of the patterns, due to, apparently, the softening of the glass substrate; while, similarly to the above cases, the remaining tungsten formed a small ring in the centre of the ablated area.

As outlined above, the trends were similar for all pulse lengths, but the peak powers specific for certain pattern types were shifted to lower values with increasing pulse lengths. It should also be noted that, except for a narrow range around the ablation power

threshold, processing with any peak power and pulse duration resulted in very reproducible patterns.

1.4.2.3. Temperature calculations and interpretation of the experimental results

To obtain quantitative insight into the laser transfer process, numerical calculations of the temperature profiles in the laser irradiated support—film structure were performed using a three-dimensional, first-order, finite difference method. The temperature dependencies of the thermophysical properties of the materials were explicitely included. The model adapted in this work assumed that the non-reflected part of the laser pulse energy was fully absorbed by the metal film; this energy absorption initiated a local temperature rise and there was tight thermal contact between the tungsten film and its support plate until ablation started.

We calculated the temperatures in the system for all pulse lengths and peak powers used in the experiments as a function of time and space. Plotting the calculated temperatures of the tungsten film in the centre of the laser spot on the time scale of the corresponding processing pulse, a characteristic temperature could be assigned to each feature appearing on the reflection and transmission signals (Fig. 16).

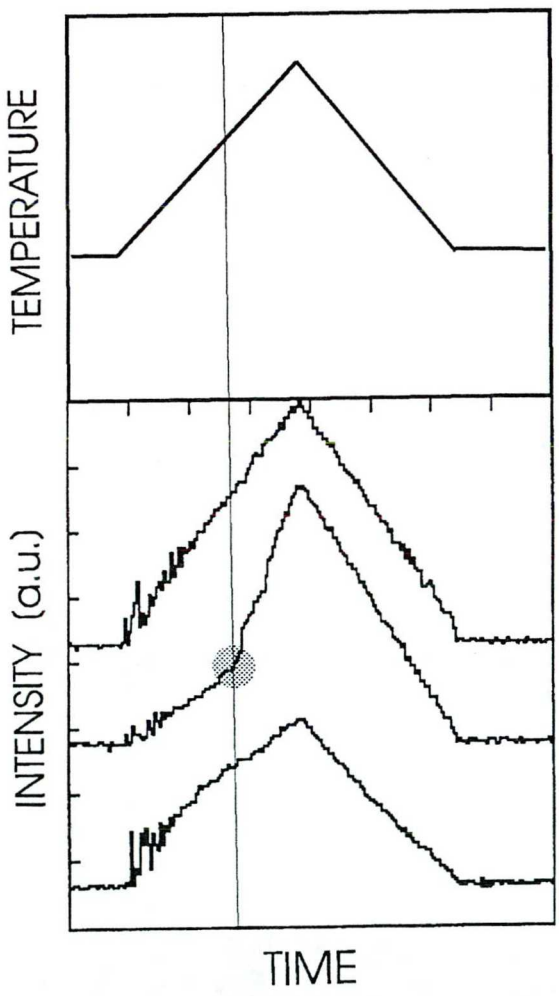

Fig. 16. An example of the method for determining the temperature at the centre of the laser spot (top panel) at the onset of the second characteristic feature of the time-dependent curves (bottom panel).

By comparing the measured reflection and transmission curves, microscopic observation of the processed surfaces and the calculated temperature data, it has been found, that for each of the the first three features, the calculated temperatures are constant regardless of both the duration and the peak power of the processing pulse, i.e. the thermal history of the sample before reaching this characteristic temperature (Fig. 17). This result suggests that the macroscopic effects determining the optical response of the processed area are of a purely thermal origin and exhibit a threshold behaviour, i.e. as the temperature in the centre of the spot reaches the threshold value, the given process starts instantaneously.

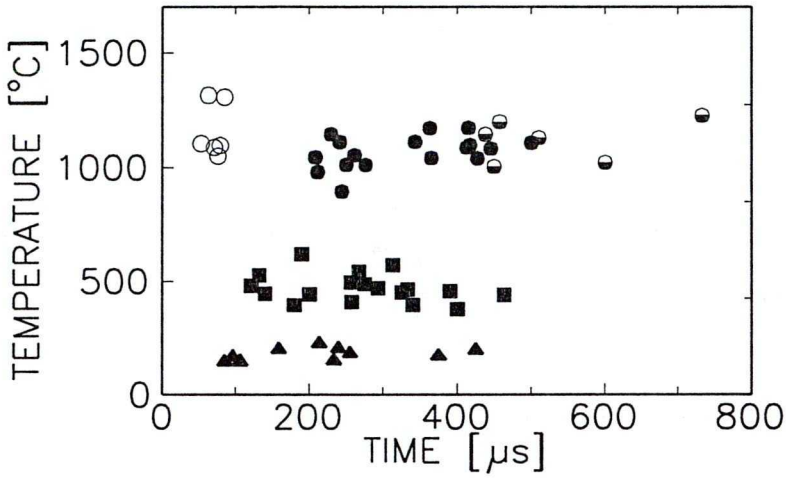

Fig. 17. Calculated central temperature values corresponding to the onset times of the first three characteristic features (see in text and Fig. 13.) of the time-dependent transmission and reflection curves for 500 μs long pulses (closed symbols). For comparison, the ablation/deposition threshold temperatures for 100 and 1000 μs pulses are also plotted as open and semi-closed symbols, respectively.

The first feature associated with the formation of uneven bulges of the metal film at low fluences (without ablation) is characterized by a threshold temperature at 210± 75 °C. The third threshold of 1120±50 °C was identified as the threshold temperature for ablation and concomitant print formation. Thus, after the onset of this third feature, the film is no longer contiguous which is consistent with the observed changes in the measured optical signals.

Microscopic examination could not detect any structural effect that could have been assigned to the second threshold temperature of 510±40 °C. The appearance of the fourth feature correlates with the damage of the central zone of the print patterns; nevertheless, the fourth feature could not have been handled in the framework of the applied model for temperature calculations since it assumed an uninterrupted thermal contact between the donor film and its original support.

The observed deviation from the linear increase after the third temperature threshold, i.e. ablation and concomitant print formation lasts 150-300 μs for 500 μs processing. This is interpreted as the total time needed for the complete transfer of the metal film over the entire irradiated area. This observation has two important consequences. First, it reveals that for transferring good-quality patterns, well adhering onto the surface over the whole area, long local laser annealing is necessary after transfer. Clearly, when processing with 100 μs pulses, there is not enough time for the completion of the transfer, which is evidenced by the broken edges of the transferred patterns

compared to those produced with 500 and 1000 μs long pulses. The second consequence is that ablation, flight and landing, can not be separated in time in the case of low power, long-pulse laser transfer. Before ablation and during transfer the heat has sufficiently long time to penetrate deeply into the support, thus the thermal expansion can easily overcome the narrow gap between the film and the target surface and the film will be pressed between the two faces, first in the centre and, then, over continuously widening area. This also contributes to the firm adherence of the patterns since contaminations on the target surface and the free surface of the film, have enough time to move outside of the hot surface due to the temperature gradients. No such "cleaning" can take place between the film and its original support, since the impurities remain trapped until the detachment of the film, leading to, apparently, weaker adhesion to the original support.

These results of the analysis of the time evolution of the long-pulse laser transfer process allowed us to optimize the material and process parameters. Because of its high melting point, tungsten proved to be an ideal material to be trasferred in solid phase from its glass support. For the actual size of the focal spot in our arrangement (8.1 μm diameter) we found that the laser pulse must be at least several hundreds of microseconds long. 500 μs long pulses proved to be sufficient for good-quality transfer of tungsten patterns, while the 1000 μs long pulses included an unnecessarily long past annealing period.

1.5. Conclusions

The critical analysis of ns-pulse induced laser transfer revealed that this process was not appropriate for micrometer resolution pattern production: high fluences resulting in melting or evaporation of the film material produced non-contiguous patterns with uncontrollable quality and dimensions, while low-fluence processing, in the regime of the clean ablation, did not ensure sufficient adhesion of the transferred patterns to the target substrate.

Dynamics of long (100-1000 μs) laser pulse induced transfer of μm-sized thin tungsten patterns was investigated. The feasibility this technique for deposition of micrometer sized metal patterns was demonstrated [28, T5, T6]. On the basis of time-resolved transmission and reflection measurements on the processed area and numerical temperature calculations we found that (i) the characteristic processes involved in long-pulse laser transfer started at well defined constant temperatures, regardless of the shape and duration of the laser pulse. (ii) With appropriate shaping of the second part of the processing pulse, on-site annealing of the deposited patterns could be attained improving its adherence to the target substrate. (iii) For these long laser pulses the conventional description of laser-induced transfer, which was based on a clear distinction between material removal, followed by its transfer and deposition, appropriate for ns-pulse processing, could not be applied. In this case the thermal expansion is comparable with the gap width between the film and target faces, and, thus, the removal phase is strongly overlapping in space and time with the transfer and adherence steps.

2. Dynamics of laser-induced synthesis of ZnSe

2.1. Introduction

A conveniently simple method for producing compound semiconductor films and patterns is the laser-induced local transformation of thin films made of a stack of elemental layers of pre-deposited elements in the appropriate atomic ratio. This method was first described by Laude et al. on AlSb some 16 years ago [54]. Using this technique, a number of other compounds have been synthesized, e.g. AlAs, CdTe, CdSe, ZnSe, $GeSe_2$, GeSe, Sb_2Se_3, GeSb, and also ternaries, e.g. $CuInSe_2$ and others [55, 56, 57, 58, 59, 60].

Similar process was described by Poate et al. for silicide formation, using the silicon substrate material as second component [61], followed by a series of other experimental papers [51, 62, 63, 64, 65]. Clearly, this local compound synthesis method is definitely simpler and less costy than other techniques like ion implantation combined with laser annealing, molecular beam epitaxy, LCVD, etc.

Although a plausible phenomenological model of the overall transformation process is drawn in Ref. [66], the separation of the anticipated individual steps of the process, namely intermixing of the layer materials, compound formation and crystallization, was calling for its experimental verification.

In this section the results of the analysis of time evolution of the film transformation are described. To this aim, multilayered films were irradiated at various power densities, over 10^{-4} to 1 s periods of time during which both reflectivity and transmission of the irradiated areas were measured by means of the laser microprocessing and monitoring system described in Section 2.3.2. Comparison of the experimental data with the result of numerical temperature calculations reveals that synthesis may develop at and above a well-defined threshold temperature, which is set by the melting of selenium. Further, it is shown that the whole process comprises three independent successive steps: inter-layer mixing (or alloying), chemical reaction (i.e. formation of an amorphous compound) and crystallization of that compound. Among other findings, this analysis shows that large atom transport velocities (on the mm/sec scale) are necessary to account for the extremely short duration of the mixing step.

2.2. Experimental

Symmetric multilayered film structures (either Zn/Se/Zn or Se/Zn/Se) were produced onto glass (soda lime) substrates by electron beam evaporation under high vacuum conditions (background pressure below 10^{-6} mbar). The elemental layers were deposited in overall stoichiometric ratio, the total thickness ranging from 50 to 150 nm. Their thickness was monitored by a vibrating quartz microbalance to 1 or 2 % accuracy.

The laser source was either an Ar^+ or a diode-pumped Nd:YAG laser, working at 514 and 1064 nm wavelength, respectively. Three different processing alignments were used.

a. In Set-up No.1, the processed area was scanned with the Ar^+ laser beam along overlapping parallel scans. The shift between consecutive scans was kept at 0.2 to 0.5 mm, with incident laser power at between 1 and 2 W. The scanning speed was set at values between 0.25 and 2 mm/s. Unshaped (TEM_{00}, 0.97 mm $1/e^2$ diameter) and elliptic laser spots were used for scanning. Larger processed areas (in the order of cm^2) were then analysed by optical spectrophotometry and X-ray diffractometry.

b. In Set-up No.2 the time course of the transformation process was examined. An electromechanical shutter was inserted along the path of the unshaped beam of the above mentioned Ar^+ laser to ensure switching of the illumination by the laser light on/off within a few milliseconds. The part of the laser light which was transmitted through the sample, was collected via a lens onto the surface of a photodiode. The obtained electronic signal was then analyzed with a digital storage oscilloscope with a temporal resolution of about 30 μs (corresponding to some 30 kHz bandwidth), essentially limited by the photodiode electronics.

c. To follow the laser-induced events taking place on a shorter time scale, the laser microprocessing and monitoring system was used as Set-up No.3. In so-doing, pre-determined pulses could be supplied with 30 μs minimum rise time, from zero to maximum light intensity. Peak power at the film surface could be set at values in the range of 20 to 230 mW. The laser beam was focused by a lens to a spot diameter of 6.4 or 8.1 μm. Before irradiation, focus control was monitored with a red diode laser and an additional focusing microscope.

The temporal evolution of the *processing pulse* itself was followed by reflecting a part of the beam onto a photodiode with a beamsplitter (see Fig. 7). The laser light which was *back-reflected* by the processed area was detected by a second photodiode whilst the laser light which was *transmitted* through the processed film was focused via a lens onto a third photodiode. The electronic signals of all three photodiodes were recorded in real time by a digitizing oscilloscope with an overall (electro-optical and electronic) transmission bandwidth of 0.5 MHz, which is a significant improvement as compared to the Setups No. 1 and 2, providing a lack of or low-resolution temporal information about the process, respectively.

2.3. Results and discussion

2.3.1. Transformation of the Zn/Se multilayer structure into ZnSe thin film by scanning laser beam (Set-up No.1)

In practice, at all scanning speeds and laser powers which were experimented in this work (0.25 to 2 mm/s and 1 to 2 W, respectively), modifications of the surface were clearly observable. The processed areas were characterized by reflection (R) and transmission (T) spectrophotometry at wavelengths ranging from 300 to 850 nm (Fig. 18). The absorption coefficient α of the transformed material was then evaluated as a function of photon energy hν. Neglecting multiple reflections at film boundaries, α can be approximated as: $\alpha = \frac{1}{z}\log\left(\frac{1-R}{T}\right)$, where z is the film thickness. On the other hand, assuming parabolic bands in the vicinity of a direct band gap (as it would be for ZnSe), the function $\eta = (\alpha \times h\nu)^2$ should evolve *linearly* with photon energy. That function η is plotted *vs.* hν in Fig. 19 for a 93 nm thick, initially Se/Zn/Se film, before irradiation (curve a) and after processing with 1 W, 1.5 W and 2 W laser powers (curves b, c and d, respectively), at 0.25 mm/s scanning speed. The linear section of the curve pointing close to 2 eV on the abscissa is related to the presence of selenium in the multilayer structure. At the higher powers, the film becomes mostly transparent over the processed area, with a yellow tone and very fine granularity as observed under optical microscope. As seen at 2 W (curve d), η remains lowest below 2.5 eV and increases linearly above, thus indicating the presence of a direct band gap at that energy [67]. At lower powers (1.5 W and 1 W, curves c and b, respectively), this peculiarity of the graph is of much less

significance as compared to the apparent high residual (non-bandgap) absorptivity. This behaviour would indicate that full transformation of the film into ZnSe would be achieved at powers exceeding approximately 2 W. Further indication of the microcrystalline nature of the transformed film is provided by grazing-angle X-ray diffractometry (Fig. 20). The ZnSe (111) diffraction peak increasing on the expense of that of the elemental (crystalline) layers is indicative of the transformation of the multilayered film into ZnSe. It should be noted that other diffraction peaks which are also characteristic of the synthesized material may not appear in the analysis, probably due to substrate-induced texturing. Further, the width of the detected X-ray diffraction peaks suggests that the characteristic grain sizes in the film are very small. Though a significant decrease of the absorptivity of this film can be observed at 1 W, curve b in Fig. 19 reveals that this laser power did not provide sufficient energy for the complete transformation of the film.

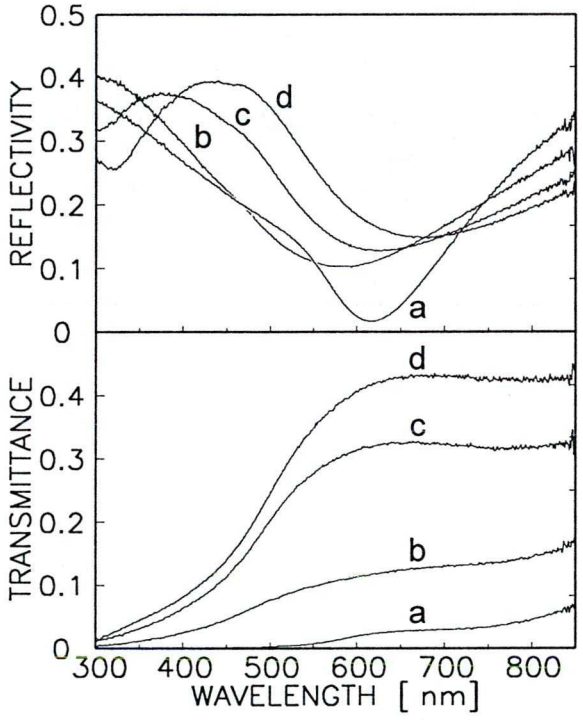

Fig. 18. Reflectivity (R) and transmittance (T) spectra of the untreated (curves a) and the irradiated areas of a 93 nm thick symmetric Se/Zn/Se structure as a function of wavelength. The processing powers were 1 W, 1.5 W and 2 W (curves b, c and d in each panel, respectively).

One may notice that there is a small signal from ZnSe present in the multilayered structure before any laser irradiation (curve a, Fig. 20). Formation of a small amount of ZnSe during the vacuum evaporation process is plausible: the first selenium atoms to reach the Zn surface may combine with Zn atoms to form an interfacial compound layer.

Increase of the processing power above 2 W is not accompanied with any remarkable improvement of the processing yield. In effect, upon synthesis, the thin film becomes transparent to the processing beam which works at 2.41 eV photon energy, i.e. below the absorption threshold (approx. 2.6 eV) of the so-formed compound.

This series of experiments revealed that microcrystalline thin film of zinc selenide could be formed from a stack of elemental layers as a result of cw laser irradiation of appropriate power and scanning speed. However, further investigations were still

necessary to understand the dynamics of the transformation process and to determine the speed of its individual steps.

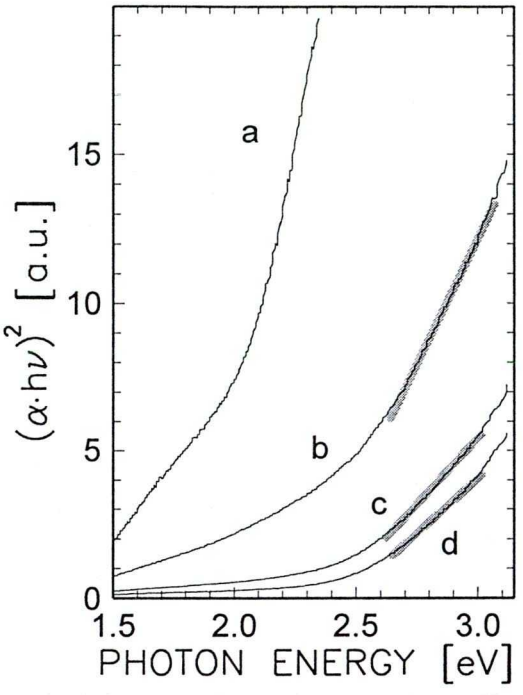

Fig. 19. Spectrophotometrical determination of the band gap of the transformed layer after laser processing. The linearity of the curves c and d reveals direct band gap at approx. 2.5 eV characteristic to ZnSe. The symmetric Se/Zn/Se structures with 93 nm overall thickness were scanned with 1 W, 1.5 W and 2 W laser powers (curves b, c and d, respectively). The curve a refers to the untreated film, from which a direct gap at approx. 2 eV can be derived corresponding to the original Se layer.

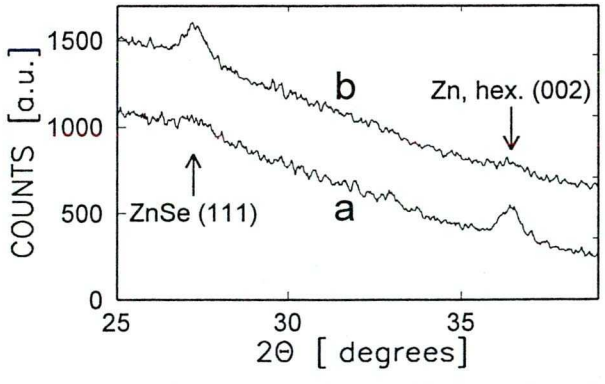

Fig. 20. Grazing-angle X-ray diffractogram of the Se/Zn/Se multilayer structure before and after treatment with scanning laser beam at 2 W laser power (curves a and b, respectively). The increasing ZnSe (111) peak on the expense of the hexagonal Zn (002) peak refers to the transformation of the elements into microcrystalline ZnSe.

2.3.2. Dynamics of the transformation: first approximation (Set-up No.2)

Real-time transmission measurements have been performed at various processing laser powers (p_L) up to 3 W. A typical transient curve is shown in Fig. 21. Characteristics of these recordings are: (i) the *spike* profile right at the beginning of the irradiation; (ii)

constant transmitted light intensity (p_T) during a time interval τ following the spike, and finally (iii) the slow rise which follows and saturates with time.

Upon increasing the laser power, p_L , both p_T and τ vary and their corresponding evolutions are reported in Fig. 22a (as τ^{-1} vs. p_L) and Fig. 22b (as p_T vs. p_L). Above a threshold (p_{thr}=0.85 W), τ^{-1} and p_T evolve linearly with p_L. It is remarkable to note that the product $\tau\times(p_L-p_{thr})$, i.e. the excess energy above threshold which is provided to (and absorbed by) the film over time τ is constant at 46±5 mJ for all irradiations.

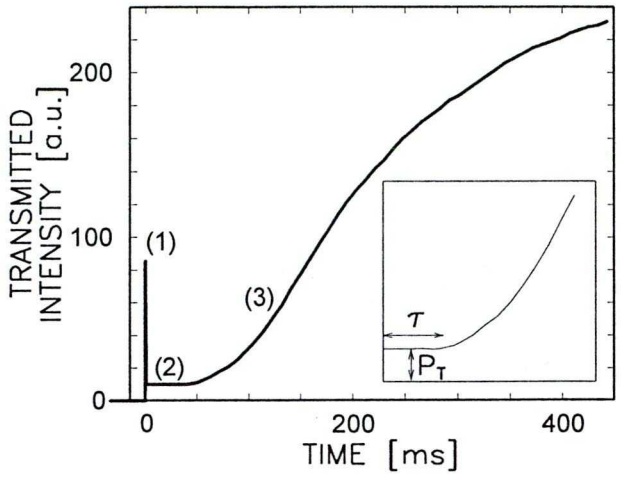

Fig. 21. The intensity of the laser light transmitted by the Se/Zn/Se structure upon irradiating with 2 W laser power. The characteristic features of such transient curves are (1) the spike profile after switching on the laser light at t = 0, then (2) the constant intensity P_T throughout a time interval τ, and, finally, (3) the slow rise.

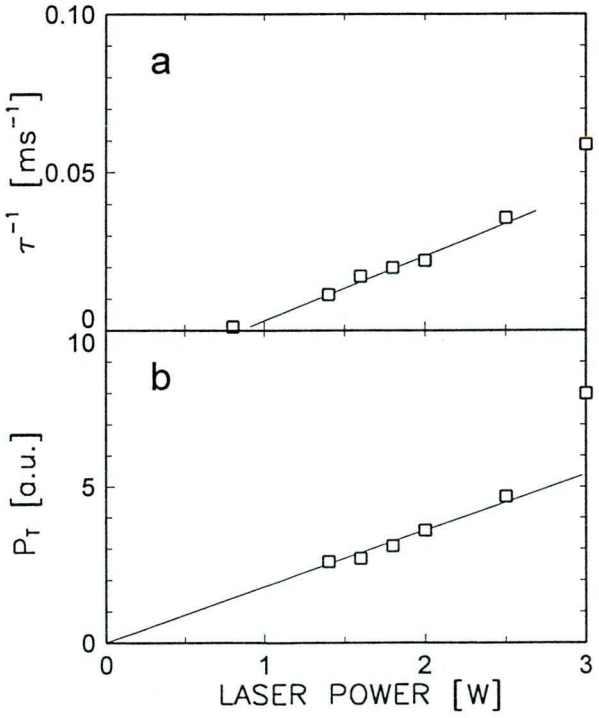

Fig. 22. The dependencies of τ^{-1} and P_T on the processing laser power. τ is the duration of the period with constant P_T intensity in the time-dependent transmission curves (Fig. 21) between the initial spike profile and the slow rise.

Although direct comparison between the results obtained with Set-ups 1 and 2 is not obvious because of the strongly different experimental conditions (scanning vs. static illumination; overlapped processing vs. one spot illumination conditions, etc.), on the base of the magnitude of the corresponding laser powers correlation could be drawn between the phases of the process distinguished in Setup 2, and the steps of the evolution of the material with increasing laser power in Setup 1.

After intermixing and chemical reaction between the elements of the pre-deposited layers (steps (1) and (2)), the slowly rising period (3) of the transmission vs. time curves in Fig. 21, can be correlated with the crystallization of the synthesized (but still amorphous) compound material.

2.3.3. Dynamics of the transformation: higher temporal resolution (Set-up No.3)

Obviously, the early spike profile detected in the measured transmission (Fig. 21) could not be resolved properly using Set-up No.2. Reasons for this poor resolution are related to both the measuring photodiode and the mechanical shutter used there. In order to learn more about the nature of this early fast process, our laser microprocessing and monitoring system was used in the following.

Upon irradiating 150 nm thick Zn/Se/Zn layer structures with Nd:YAG pulses of 50 mW peak power (focus diameter at 8.1 μm), for any rise time between 50 and 500 μs from zero to constant maximum, the recorded transmission and reflectivity curves exhibited certain characteristic features, such as decreasing and increasing periods. The

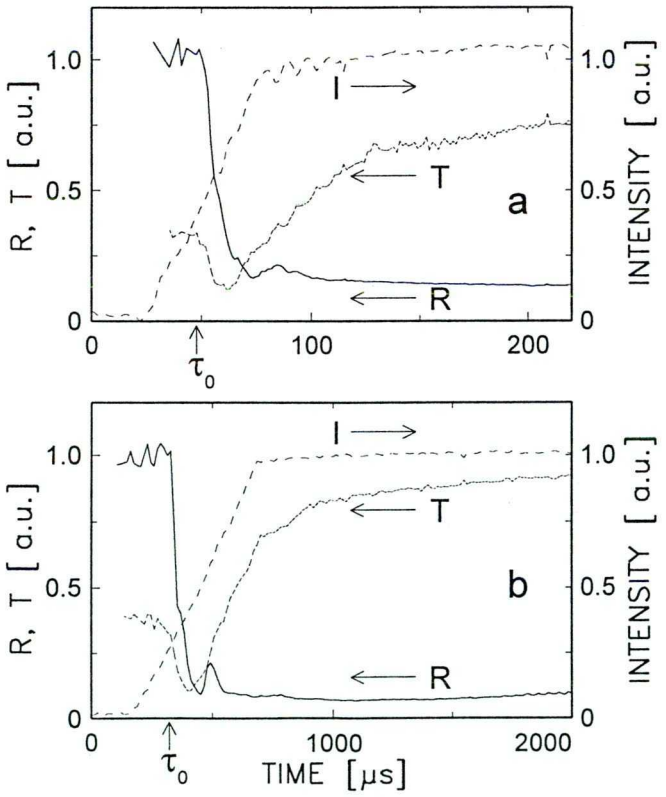

Fig. 23. Transmittance (T, dashed lines) and reflectivity (R, solid lines) during Nd:YAG laser processing of 150 nm thick Zn/Se/Zn layer structures as a function of time. The time course of the processing laser intensity is plotted with dotted line (I). All quantities are given in independent arbitrary units. The rise times of the laser intensity were 50 and 500 μs (a and b, respectively), the peak power being 50 mW for 8.1 μm focus diameter.

lowering of the rise time, i.e. increasing the energy injection rate systematically led to an increase of the rates of the optical changes. Typical curves of reflectivity and transmittance, measured at the centre of the irradiated film are shown in Fig. 23a and 23b for 50 and 500 μs rise times, respectively.

In the first period of the irradiation, both the reflectivity and transmittance remain constant at respective values which are characteristic of Zn, forming the outer surface of this film. A sudden drop of both curves is then observed at τ_0. After reaching a minimum value, the transmission turns to increase and then stabilizes with time. In contrast, reflectivity reaches a minimum, increases for a short period and decreases again to approach a finite but lower value. Qualitatively similar reflectivity curves have been reported by Kolev et al. [66] during the laser-induced synthesis of Sb_2Se_3 films, though on a different time scale resulting from different irradiation conditions.

During irradiation, the temperature of the multilayered film increases. The spatio-temporal evolution of that temperature has been calculated and plotted for each processing. Considering the long rise times of the irradiation pulses, the temperature was treated to be constant within the whole thickness of the elemental layer structure. Further, tight thermal contact between the multilayered structure and the underlying substrate was assumed. The thermal conductivity equation was solved numerically using a two-dimensional, first-order finite difference scheme. The actual film temperature at the centre of the processed area at time τ_0 (Fig. 23), marking the start of the decreasing period of the recorded optical signals is plotted in Fig. 24 as a function of τ_0. That temperature is found to be practically constant at around 525±25 K, i.e. just above the melting point of selenium (reportedly at 487 K), *whichever the irradiation scheme*. Therefore, it would seem convincing to propose that the whole synthesis process stems from the actual melting of selenium which, among the two elements present in the film, is the one exhibiting the lower melting point (Zn melts at 692 K). Reasonably, one would associate the first drop in reflectivity to the emergence of Se in the vicinity of the film outer surface, which would start at τ_0 and stabilize some 20 or 100 μs later (Fig. 23a or b, respectively). This hypothesis is further supported by the fact that films were not affected by low-power pulses at which the maximum film temperature could not reach this threshold value.

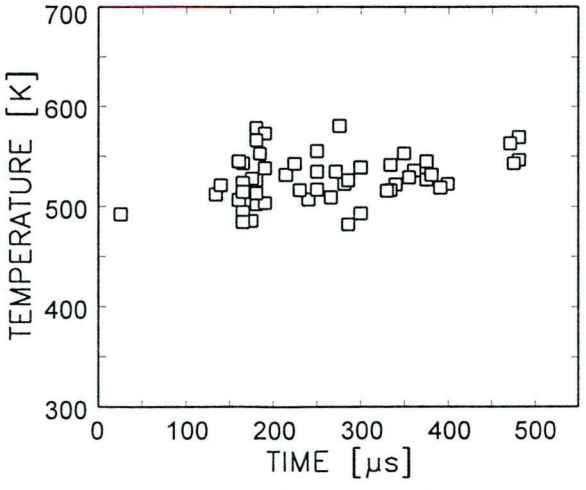

Fig. 24. Calculated temperatures of the Zn/Se/Zn thin film structure at the centre of the irradiated area, corresponding to the point of time of the onset of the steep decrease of the time-dependent transmission and reflectivity curves (Fig. 23). The temperature values scatter in a narrow domain around approx. 525 K, which suggests that the first changes are bound to the melting of selenium. The heating rate was varied by changing the rise time of the laser pulse.

Over this 20 (or 100) μs period of time, the intermixing process develops and saturates. The resulting material could be considered as a transient (unstable) metallic Zn—Se liquid alloy. Taking into consideration the thickness of the multilayered film, average atom transport velocities amounting to several mm/s can be immediately derived which are effectively characteristic of atom migration in the liquid phase. However, as selenium penetrates the adjacent Zn layers, concentration (and chemical potential) gradients decrease, thus reducing atom velocities as well. Thereby, the capture cross section of the Zn atoms with respect to the selenium ones increases and chemical reaction (i.e. the forming of covalent Se—Zn bonds) starts. At that stage of the process, an amorphous compound would tend to develop at random in the transient alloyed film. Given the covalence of the Se—Zn bonds, the amorphous compound formation (i.e. its synthesis) results in a decreased optical absorption, i.e. an increasing transmittance already *before* completion of the homogeneous distributions of Se and Zn atoms in the film. As derived from the curves in Fig. 23a or b, the characteristic duration of this process is about 25 or 100 μs, respectively.

Similarly to the case of processing with the static Ar^+ laser beam (Section 3.3.2., Fig. 21), the slow rise of T and decrease of R can be assigned (i) to the completion of the synthesis process, and (ii) to the (slower) crystallization process developing in the now formed amorphous compound layer [66]. An analysis of this part of the curves in Fig. 23a and b reveals exponential evolutions with actual time constants on the order of cca. 55 and 630 μs, respectively.

It should be noted that, on the base of their real-time temperature measurement experiments, Hanus and Wautelet could also associate temperature threshold values to the onset of laser-induced compound formation, but they concluded that formation of CuTe, Cu_7Te_5 and Cu_2Te takes place in the solid phase [68]; taking into account the temperature calibration method they used, the temperature values quoted there seem to be underestimated, i.e. the real temperatures may approach the melting point of tellurium.

2.4. Conclusions

Laser-induced synthesis of ZnSe film from multilayered elements was demonstrated. As evidenced by optical microscopy, spectrophotometry and X-ray diffractometry, the reaction product is microcrystalline zinc selenide.

The analysis of real-time reflectivity and transmission measurements has shown, that the overall process consists of three phases. The first one is fast intermixing between the film materials triggered by the melting of the selenium and, thereby, bound to exceeding a threshold temperature. The second phase is chemical reaction between Zn and Se atoms, which transforms the unstable mixture into amorphous compound. Finally, the layer undergoes a relatively slow crystallization process. Upon increasing the processing power, the particular processes take place with higher rates.

The mechanism of this synthesis was investigated on the time scale ranging from one second down to few tens of microseconds. In this range we did not observe saturation of the speed of the particular reactions with increasing heat injection rate, thus possibility of further shortening of the total processing times can be expected [69]. If so, this technique can be useful for optical data storage with reasonable recording speed [70]. Among the high contrast ratio in reflectivity achived by application of such semiconductor compounds as compared to the generally used, Al-based optical compact disks (CD) [71], the future application of ZnSe diode lasers for both recording and reading, i.e. shorter wavelengths in the blue may allow lower dimensions of the data bits, resulting higher data

density. However, substitution of the conventional media with the new material is rendered more difficult because of the demand of the standard min. 70% reflectivity of the non-recorded areas.

3. Excimer laser-induced ablation of transparent conductive oxides

3.1. Introduction

3.1.1. Applications of transparent conducting materials

Partial transparency and fairly good conductivity may be obtained in very thin films of a variety of metals, but these thin films are usually rather fragile and possess poor chemical stability.

The simultaneous occurrence of high optical transparency in the visible region and high electrical conductivity is not possible in intrinsic stoichiometric oxide materials. The only way to obtain good transparent conductors is to create electron degeneracy in wide band-gap (>3 eV) materials by controllably introducing non-stoichiometry and/or appropriate dopants. These conditions are very conveniently obtained in oxides of cadmium, tin, zinc and their alloys in thin film form, prepared by a number of deposition techiques. Ever since the first report of transparent conducting CdO films prepared by the thermal oxidation of sputtered cadmium by Badeker [72] the technological interest in transparent conductors has grown tremendously. Numerous techniques for depositing several very useful transparent conducting oxides, notable tin oxide (TO), antimony-doped indium oxide (ATO) or fluorine-doped tin oxide (FTO) and tin-doped indium sesquioxide (ITO) have been developed, some at a large-scale production level. Other transparent conducting materials are cadmium stannate (CTO), indium sesquioxide (IO), zinc monoxide (ZO), and some recently developed materials such as $Zn_2In_2O_5$, $ZnSnO_3$ and $GaInO_3$. Specially treated transparent polymeric materials also possess noticable electrical conductivity [73].

High visible transparency (above 80%) and infrared reflectivity, high electrical conductivity (about $10^3\ \Omega^{-1}cm^{-1}$) and good mechanical and chemical resistance invoked many electronic, opto-electronic and mechanical applications based on transparent conductors. In order to give an impression to the reader, without listing numerous references, I only mention that these thin film devices are applied as resistors, interconnects in microelectronic devices and contacts on high-T_c superconductors; transparent heating (deicing) elements for aircraft and automobile windows; antistatic coatings for instrument windows; touch-sensitive coatings on interactive information displays; electromagnetic shieldings, thermal isolation of windows and buildings, heat reflecting layers for improved efficiency of incandescent bulbs; antireflection coatings; selective absorber components of solar heat collectors; electrodes for liquid crystal, electrochromic, ferroelectric or magnetic storage and display devices; electrodes of charge coupled and charge injection imaging devices; vacuum fluorescent displays and thin film electroluminescent displays; transparent electrodes (and antireflection coatings) of various types of solar cells, contacts of diode lasers, semiconductor/insulator/semiconductor (SIS) heterojunctions; thin film transparent thermocouples; moisture and oxygen resistant coatings, protective and wear-resistant coatings for glass containers etc. Furthermore, thin tin oxide films are often used in chemical sensors due to the variation of its electrical conductivity with the oxygen and alcohol concentration of the environment.

3.1.2. Preparation of transparent conducting thin films

A variety of thin film deposition techniques have been employed to deposit transparent conducting oxides. Since the optical and electrical transport properties in these films depend strongly on their microstructure and stoichiometry and the nature of the

impurities present, each deposition technique with its associated parameters yields films of different properties.

Depending on the deposition technique, the substrate may have a significant influence on the properties of the films. Glass substrates are most commonly used. In the case of high-temperature deposition techniques (e.g. spraying, dipping or screen printing including quenching or sintering processes) the thermal expansion of the substrate plays an important role by inducing intrinsic stresses in the films. Moreover, for ZnO films the thermal expansion coefficient was also reported to affect the preferred orientation of the crystallites. At high temperatures diffusion of impurities from the glass substrate, e.g. sodium has to be taken into account or be avoided by depositing an interlayer as diffusion barrier. Low-temperature deposition techniques, such as magnetron sputtering, ion beam sputtering and reactive ion plating allow the deposition of the conductive oxide films onto polymer or other heat sensitive surfaces.

Preparation method	Materials
simple thermal evaporation (under low-pressure O_2)	IO
(activated) reactive evaporation	IO, TO, ITO, ZO, ATO
direct sputtering from oxide target	TO, ATO, IO, ITO, ZO, CTO
atom or ion beam sputtering	TO, ITO, MoO_3, CTO
reactive sputtering	IO, CTO, CdO, TO, ATO, ITO
reactive magnetron sputtering (DC or RF)	ITO, ZO:Al, :In $Zn_2In_2O_5$, $ZnSnO_3$
reactive ion plating	ITO
spray pyrolysis of solutions and melts	TO (:Cl, :F, :Sb), IO, ITO ZO (:Al, :In)
Pyrosol technique (= *pyro*lysis of an aero*sol* produced by ultrasonic spraying)	IO, ITO; TO (:F) Fe_2O_3
dip coating	TO, ITO, ZO:Al
oxidation of a thin film of the respective metal or a precursor compound	CdO, ZO, TO, IO, ITO
chemical vapour deposition from $SnCl_4$ and organometallic compounds	TO, ITO, ZO (:Al)
deposition from gels	ITO, WO_3
high-temperature solid-state synthesis	ITO
screen printing + sintering	ITO
laser chemical vapour deposition	TO
pulsed laser deposition	ITO

The most important film preparation methods are compiled in the table above. To achieve the desired optical and electrical properties, some of the deposition techniques listed above are sometimes combined with subsequent thermal annealing under controlled atmosphere.This list is not exhaustive (for an earlier review, see also [74]), and due to the continuous research activity, the set of the available deposition techniques is steadily broadening.

Sputtering is one of the most extensively used techniques for the deposition of transparent condicting oxide films. dc ('direct current') and rf ('radio frequency') sputtering, as well as magnetron, ion beam and neutralized ion beam sputtering have been used. Non-reactive and reactive (i.e. direct) sputtering can be distinguished, for as much as

the sputter target is the oxide material to be deposited itself, or a metal piece or a mixture or an alloy of the corresponding metals, while the oxygen present in the sputtering gas (or beam) is used for the formation of the compound. Direct sputtering from oxide targets (hot pressed, pure or mixed oxide targets) renders good control over the stoichiometry, thus in most cases post-deposition heat treatment is not necessary. However, while layers deposited onto cold substrates tend to be amorphous, increasing the substrate temperature in the range 150—500 °C during deposition improves the crystallinity and grain size and increases the carrier mobility. Addition of oxygen to the sputtering gas (usually argon or nitrogen) at low partial pressure also improves the quality of the deposited films.

3.1.3. Patterning techniques

Since the transparent conductive oxides can most conveniently prepared over large areas, subsequent patterning of these films is often necessary. Photolithographical lift-off processes are hardly performed homogeneously over large areas, while wet chemical etching is hindered by the fairly good chemical resistivity of the most commonly used transparent conductors. However, only those etching agents may be applied that do not attack the parts of the device underneath the film. Therefore neither nitric acid or alkaline solutions can be used, while with e.g. H_2SO_4 and HCl only low etching rates can be obtained. Recently, reactive ion etching was shown as an important candidate for high-resolution patterning of SnO_2 and ITO layers [75].

On the other hand, while the deposition of such materials is no longer restricted to two dimensions (e.g. the dipping technique), lithographic techniques, practically, are unable to handle rather large and curved structures.

Production of structured layers can follow two basic ways: either selective deposition of the material, or post-deposition patterning of a homogeneous thin layer. Among the conventional lithography, in our aspect, laser-assisted methods are of most interest.

Selective area photodeposition of transparent conductive SnO_2 film has been demonstrated by Kunz et al. [76]. Due to ArF excimer laser-induced photochemical reactions in $SnCl_4/N_2O$ atmosphere, 100 nm thick SnO_2 thin film patterns have been produced, with a lateral resolution of approx. 10 μm. The maximum temperature of the substrate during the LCVD process was estimated to remain below 400 °C, i.e. the thermal damage is negligible. Without any subsequent annealing, the deposited material was found to be of high electrical conductivity, with a transmission cut-off wavelength of approx. 330 nm.

Recently, promising experiments of deposition of transparent conductive oxide materials from liquid-phase precursors have been performed by Geretovszky et al. [77]. Pyrolytic deposition of SnO_2 from alcoholic—aquaeous solutions of $SnCl_4$ was obtained by the laser direct writing technique using a continuous wave multimode argon ion laser as heat source. The spatial resolution in their configuration was on the 10-μm scale.

Laser patterning of pre-deposited transparent conductor layer was investigated as a fabrication method for integrated-type a-Si solar cell submodules by Nakano et al. [78]. The authors report on selective evaporation of a transparent conducting oxide (TCO) layer by a scanning beam of a pulsed Nd:YAG laser at 1064 nm wavelength, without effective modification of the underlying amorphous silicon or glass. Optimum laser power densities were calculated from a three-dimensional thermal analysis and confirmed by the experiments. Unfortunately, this analysis can hardly be compared with other numerical calculations (see e.g. Ref. [79]) because the transparent conductor layer is referred simply

as TCO and, apparently, represented by only one set of thermophysical parameters, while, as shortly mentioned, it is rather an ITO/SnO_2 bilayer structure.

Excimer lasers which deliver UV pulses of several 10 ns duration offer a straightforward approach to high resolution surface structuring with a minimum of undesirable thermal and mechanical effects beyond the processed volume [79, 80, 81, 82]. Comparing the results of different research groups with our experiments, it became apparent that ablation of thin films is markedly different from that of homogeneous bulk materials [T10, T11, T12, T13]. From this point on, ablation of transparent conductive oxides, such as tin oxide and ITO was not only (and not first of all) a technical problem for us. These oxides became also model materials for investigating the question: what are the unique properties of supported thin layers upon exposition to intense laser radiation as compared to the bulk material.

3.2. Atypical features of ablation of supported thin films

In most cases material removal is the result of simple thermal processes (e.g. evaporation), or at least, the local temperature increase due to light absorption plays a decisive role in initiating the process. Clearly, in these cases the thermophysical properties of the material(s) within the thermally affected volume determine the ablation characteristics.

Upon ablating homogeneous bulk samples these material parameters are constant in the whole heated volume. As long as the thickness of the remaining material is orders of magnitude larger than the thermal diffusion length, consecutive laser pulses impinge on practically identical surface resulting in ablation characteristics independent of the number of shots. It is worth to note that originally the term *ablation* was used in this sense.

However, in the case of supported thin films, materials with different thermophysical properties are interfaced, resulting in ablation characteristics to be markedly influenced by the discontinuous material properties at the film-substrate interface. In Section 1.2.3.2. clean ablation of metal films was discussed as a direct consequence of the strikingly dissimilar optical, thermal and mechanical properties of the thin film and the substrate material. Nevertheless, in recent publications [T11, T10] it was shown that some wide band-gap semiconductor materials, especially thin tin oxide and indium-tin oxide films exhibit rather similar behaviour upon pulsed excimer laser irradiation, even though these oxides possess e.g. optical properties much close to those of the underlying glass substrates. The comparison of these results with those of the experiments on metal film ablation made it clear that nanosecond-pulse induced clean ablation must be a general feature of supported thin films of thicknesses within the limits of the actual thermal diffusion length. Moreover, our systematic laser ablation experiments with the above mentioned oxides have shown that increasing the film thickness results the ablation characteristics to be gradually approaching to those of the homogeneous bulk material.

3.3. Experimental

Commercially available, 350 and 820 nm thick tin oxide films and 70, 160, 400 and 500 nm thick dc sputtered indium-tin oxide films (provided by Sully Produits Spéciaux, France) on glass substrates were exposed through a contact metal mask to spatially homogenized single pulses from a Lambda Physics LPX 110i KrF excimer laser (λ=248 nm, 23 ns FWHM). Rectangular areas between approx. 2x2 and 10x10 mm^2 were illuminated with consecutive single pulses of constant energy distribution within 5% over

the total area using a beam homogenizer (SOPRA, Bois-Colombes). Pulse energy density was adjusted between 20 and 1800 mJ/cm^2 on the sample surface by changing the output pulse energy and/or the dimensions of the processed area. Higher fluence processing was done by directly focusing the beam onto the sample surface with a single cylindrical lens. Due to experimental inaccuracies in measuring pulse energy and spot dimension, uncertainty in the fluence values which are quoted in this work is estimated to be 20%. The topography of the processed areas was recorded by a VEECO Dektak 3030 ST surface texture analysis system, while changes in surface morphology were followed by optical microscopy.

3.4. Tin oxide films on glass

The variation in ablation depth per pulse with laser fluence for tin oxide films of thicknesses varying from 200 to 2500 nm is shown in Fig. 25. Our experimental results of

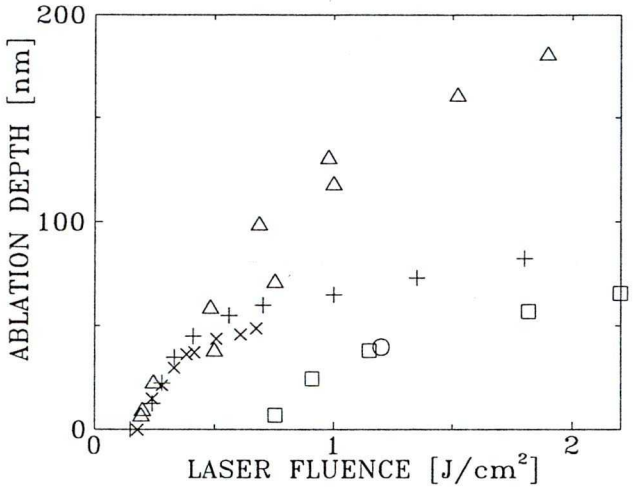

Fig. 25. Ablation depth per pulse as a function of laser fluence for tin oxide films of thicknesses (O) 200 nm [81], (×) 350 nm, (□) 430 nm [79], (+) 820 nm and (△) 1000-2500 nm [80].

350 and 820 nm thicknesses were measured as the depth of the ablation patterns produced with single shots onto untreated film surface, i.e. real first-shot ablation depth values. These experimental points are shown together with imported etch rate data calculated as depth per number of pulses (claiming that the etch depth is a linear function of the number of pulses). [79, 80, 81] The ablation thresholds for 350, 820 and 2500 nm thicknesses are remarkably similar: 200±10 mJ/cm^2. Typical of the ablation curves the depth steeply rises with fluence from the threshold region up to about 600 mJ/cm^2 for 820 and 350 nm thicknesses and up to about 1.7 J/cm^2 for 2500 nm thickness. In the case of higher fluences the slope of the curves decreases. This saturation is due to the shielding effect of the escaping material within the duration of the processing pulse. It is apparent from Fig. 25 that there are great differences in depth values at high fluences. In our experiments typically 3x3 mm^2 squares were ablated; Koinkar and Ogale [80] did not specify the dimensions of the processed area but from the description of their experimental arrangement and reported fluence data significantly smaller processed areas are estimated. As pointed out by Eyett and Bäuerle [83] the ablation rates strongly depend on the processing spot size. Especially, ablated species at high speed can escape from small processing areas sideways before the end of the laser pulse, unlike the case of large-area processing (our case) where the ablated material being above the illuminated area still

represents a significant absorptivity, i.e. shielding effect against of the processing laser light, thereby reducing the attainable ablation depths; this effect can explain the deviation. Comparing the above three sets of data and that reported by Meringdal and Slinde [81] (Fig. 25) it can be concluded that with decreasing film thickness the attainable ablation depth decreases. It should be noted that the ablation curve reported by Lunney et al., [79] follows a rather distinct trace.

The time evolution of temperature profiles was calculated for the film thicknesses discussed above and fluences between 150 and 3600 mJ/cm^2. The temperature-induced changes in the material are revealed by the maximum temperatures attained during processing. In Fig. 26 calculated maximum temperatures are plotted as a function of the depth measured from the tin oxide-air boundary for 1 J/cm^2. As seen, consistently with the experimental findings, the thickness of the layers of temperatures exceeding a given threshold increases with increasing film thickness. This trend is obvious for thicknesses comparable to and below the thermal diffusion length. For film thicknesses above ≈1 μm the temperature distribution near to the film surface is practically not influenced by the thickness. This is the consequence of that the glass support acts as a heat sink. These tendencies apply to all fluences investigated.

When processing the tin oxide film of 820 nm thickness with pulses above approx. 1.5 J/cm^2 the layer is cracked and ripped off from the substrate over the illuminated area, forming an array of separated, irregular islands, still remaining on the surface. Just above 1.5 J/cm^2 this phenomenon is of statistical nature, which becomes typical with increasing fluence. For 350 nm thickness this phenomenon takes place already above approx. 700 mJ/cm^2.

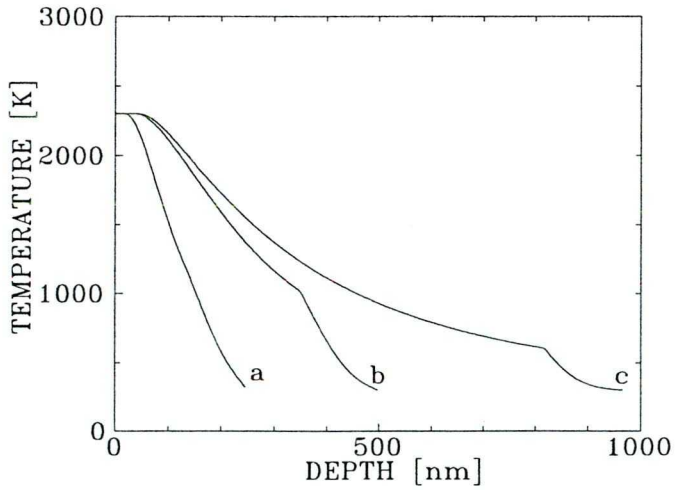

Fig. 26. Calculated maximum temperatures as a function of depth measured from the tin oxide-air boundary for (a) 100, (b) 350 and (c) 820 nm film thicknesses the processing fluence being 1 J/cm^2.

The result of processing with pulses above the ablation threshold is the evaporation of a surface layer (i.e. ablation) and concomitant melting of the underlaying one. Following the propagation of the resolidification front there is a build-up of elastic tensions. At sufficiently high fluences the mechanical strength of the film material can not withstand such elastic tensions and the system relaxes via extensive crack formation. As the shearing forces at the film-support interface overcome adhesion, the film detaches from the support resulting in the above described island-like peel off. The larger the film thickness, the more likely that the elastic forces relax within the partial thickness. This

explains why the threshold fluence for this ripping-off effect is shifted to higher values with increasing thickness.

The technological importance of this phenomenon is, that because of the thermal decoupling of the film subsequent pulses can evaporate the film material more efficiently thereby reducing the number of pulses necessary for complete film ablation.

3.5. Indium-tin oxide films on glass

3.5.1. Results

Low fluence ablation characteristics of ITO films of thicknesses ranging from 70 to 500 nm are shown in Fig. 27. The data represent the depth of the ablation patterns produced with single shots onto an untreated film surface.

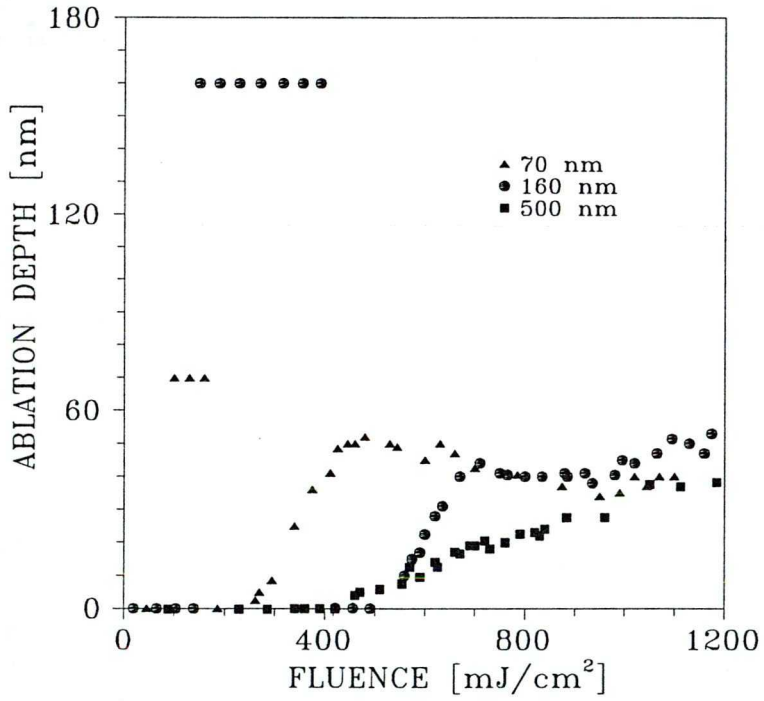

Fig. 27. Ablation depth per pulse as a function of laser fluence for 70, 160 and 500 nm thick indium-tin oxide films

70 nm film

For 70 nm thickness, irradiation with single pulses at a fluence between 100 and 160 mJ/cm^2 results in complete removal of the oxide film from the support over the whole irradiated area. The edges of the ablated pattern and those of the removed piece(s) are of abrupt contours, suggesting that in this clean ablation window ablation starts by ripping off solid-phase material. The appearance of tiny droplets of 0.4-0.6 μm dimension and rough, resolidified surface reliefs sets the upper fluence limit for this highly efficient ablation mechanism. Ablation is re-activated above a second threshold, at 260±10 mJ/cm^2. The ablation rate steeply increases with fluence from the threshold region up to ~50 nm. When reaching this value, the ablation rate saturates and then even slightly decreases above it.

160 nm film

In the case of the 160 nm thick layer the scenario remains essentially the same with a shift of the thresholds to higher fluences. The clean ablation window broadens and extends now from ~150 to ~390 mJ/cm^2. The second ablation threshold lies here at 520±20 mJ/cm^2. Note that this value has been derived from a semilogarithmic plot of the rising part of the ablation curve, since the resolidified, uneven surface renders the determination of the ablation depth values rather inaccurate just above ablation threshold. At around 700 mJ/cm^2 the ablation depth reaches a plateau, and starts increasing anew at around 900 mJ/cm^2.

400 and 500 nm films

These thick ITO films proved to have identical ablation characteristics, within experimental error. As seen in Fig. 27, these characteristics are, however, remarkably different from those obtained for the lower thicknesses. The clean ablation window disappears and layer-by-layer ablation starts at ~430±10 mJ/cm^2. The data exhibit now the typical behaviour of bulk ablation.

3.5.2. Discussion

The above experimental results for ITO films convincingly demonstrate striking differences in their ablation characteristics as a function of thickness. In the low fluence domain, which has been covered in this work, the ablation depth (at any given fluence) decreases with increasing film thickness, and concomitantly the fluence thresholds shift to higher values as shown in Fig. 27.

The particularity of the thinner films (70 and 160 nm) is the possibility of complete removal of the whole film material with a single, extremely low fluence pulse. The existence of such clean ablation windows has been evidenced elsewhere for thin metal films [46, 34, T2, T3, T4]. Clean ablation, in the case of ITO films, is rather surprising because ITO films are considered to be extremely well adhering to the glass substrate. It is needless to stress that since this effect is insensitive to fluctuations in the fluence over a wide range, i.e. exact setting and strict control of the laser parameters is not necessary, and the ablated pattern faithfully reproduces the illuminated area, processing in this window provides a highly efficient and convenient means for one-step, large-area surface patterning.

3.5.3. Modelling

To obtain a consistent explanation of the experimental results outlined above, the evaluation of temperature profiles was performed using a mathematical, finite difference method (i.e. local thermodynamic equilibrium approximation) taking into account the temperature dependence of thermophysical data and incorporating phase changes, at fluences in the range of 0 to 2 J/cm^2, for each thickness. (Concerning the method, see Refs. [T2], [53] and the Appendix.) The nominal composition of the ITO films being 90% In_2O_3—10% SnO_2, the material parameters needed in the calculations have been approximated from In_2O_3 data in the literature. Since the latter data exhibit a rather large uncertainty [67, 84, 85, 86, 87] the following set of parameters was used in the calculations:

α@248nm, In_2O_3,	$2.2 \cdot 10^5$ cm^{-1} [88]
α@248nm, In_2O_3, gas	$6 \cdot 10^5$ cm^{-1} *
α@248nm, glass	10^5 cm^{-1} **
κ, In_2O_3	5.65 $Wm^{-1}K^{-1}$ [84]
κ, glass	$(1.71 \cdot 10^{-3} \cdot T[K]+0.6)$ W $m^{-1}K^{-1}$ [85]
c_p, In_2O_3 (solid)	$(340.5+0.0904 \cdot T[K])$ J $kg^{-1}K^{-1}$ [67]
c_p, In_2O_3 (melt)	521.3 J $kg^{-1}K^{-1}$ *
c_p, glass	$(0.275 \cdot T[K]+587.5)$ J $kg^{-1}K^{-1}$ [85]
T_{melt}	2300 K ***
$T_{evaporation}$	3600 K [67]
L_{melt}	301.4 kJ kg^{-1} [67]
$L_{evaporation}$	1281 kJ kg^{-1} [67]
ρ, In_2O_3	7120 kg m^{-3} [87]
ρ, glass	2760 kg m^{-3} [85]

* Fit parameter.
** Derived from measured ablation characteristics of the glass support.
*** BALZERS Product Info (1993/1995).

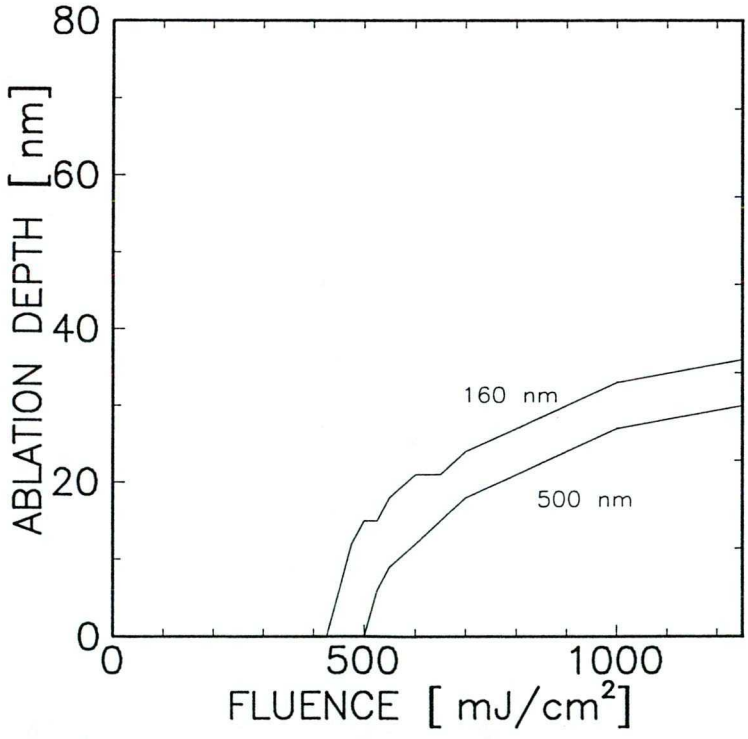

Fig. 28. Calculated ablation depth as a function of laser fluence for 160 and 500 nm thick indium-tin oxide films

The calculated ablation depth *vs.* fluence functions are shown in Fig. 28. Despite the crude approximations, the calculated curves qualitatively describe the measured

behaviour. The ablation depth decreases with increasing film thickness, and the ablation threshold for 70 nm is lower than that for 160 nm. At high fluences, the absolute values of the ablation depths fit fairly well.

From an estimation of the maximum temperature of the ITO/glass interface as a function of fluence, Fig. 29, it is obvious that in the case of the two thinner films, the interface and consequently the whole film, reaches remarkably high temperatures even for relatively low (below predicted ablation threshold) fluences. In contrast, for 500 nm film thickness, this temperature remains below 600 K even when ablation of the uppermost layer starts. In the former case(s) the elastic tensions rising at the interface due to the elevated temperatures can exceed adhesion strength, while in the latter case(s) they remain too weak to compete with adhesion forces.

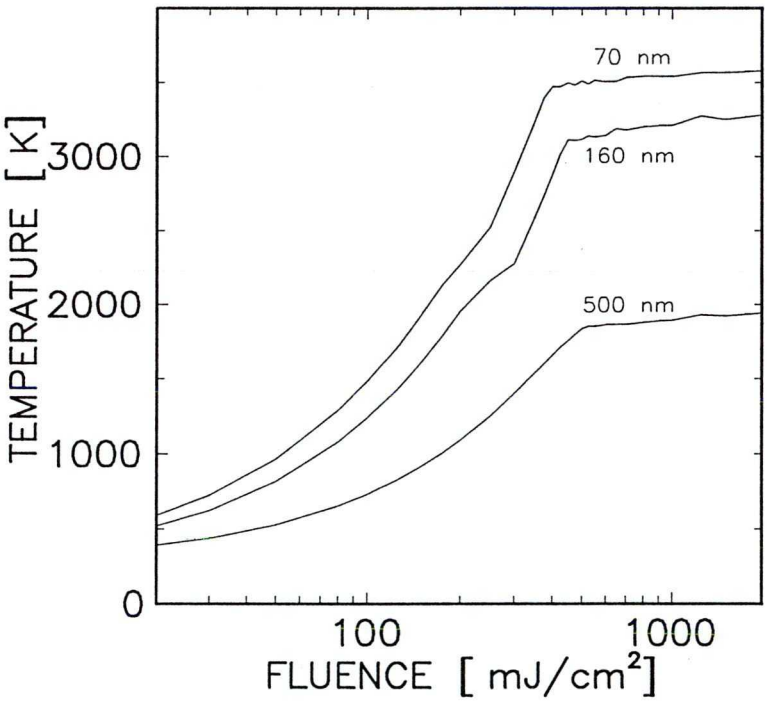

Fig. 29. Calculated maximum temperatures at the ITO/glass interface as a function of laser fluence for 70, 160 and 500 nm thick indium-tin oxide films.

As it was already mentioned, there exist contradictory thermophysical data for ITO. Upon analysis, the formerly anticipated sublimation of the material (see in Ref. [T10]) could be excluded because this assumption led notoriously to too low values for the second (evaporative) ablation threshold. A second evidence of melting was the appearance of droplets at the upper limit of the clean-ablation fluence range. Further investigations showed that melting is accompanied with In_2O_3/SnO_2 phase segregation at temperatures below ablation, followed by the selective ablation of the tin sub-oxide constituent, i.e. non-congruent ablation, leaving on the substrate pure indium oxide in the form of molten droplets. On the other hand, the satisfactory agreement between calculated and measured data far from the second ablation threshold suggests that at higher fluences congruent ablation of In_2O_3 becomes the dominant and single ablation mechanism.

3.5.4. Incongruent ablation of 500 nm thick ITO films

Darkening of ITO films during preparation [89, 90], in glow-discharge plasmas of hydrogen and argon [91, 92], and in high temperature hydrogen atmospheres [93] is a well known phenomenon, attributed to reduction.

Excimer laser processing induced also color changes that varied with processing fluence and could not be accounted for interference effects [T12, T13, 94]. For the 500 nm thick ITO films, which did not possess clean ablation, this discoloration was observed also at lower fluences, below the (evaporative) ablation threshold.

The laser-induced absorption spectra (i.e. the difference between the absorptance values of the laser-processed film and those of the unprocessed film, as a function of photon energy) were deconvoluted into four Gaussian-profile absorption bands, centered at 0.7, 1.0, 1.6 and 2.6 eV photon energy (referred as Gauss #1 to 4, respectively). The integrated peak areas of each Gaussian components are plotted in Fig. 30 as a function of processing fluence. Being absent in the original films and emerging in optical spectra at fluences exceeding 300 mJ/cm^2, the 2.6 eV contribution is most characteristic to excimer laser processing and is responsible for the darkening of the film. Taking into consideration the results of additional X-ray photoelectron spectroscopic (XPS) analysis and electrical resistivity measurements [T12, T13], the defect responsible for this absorption band can be identified most likely as a neutral ternary complex, $SnIn_2O_4$, which was formed via oxygen displacement within the atomic matrix.

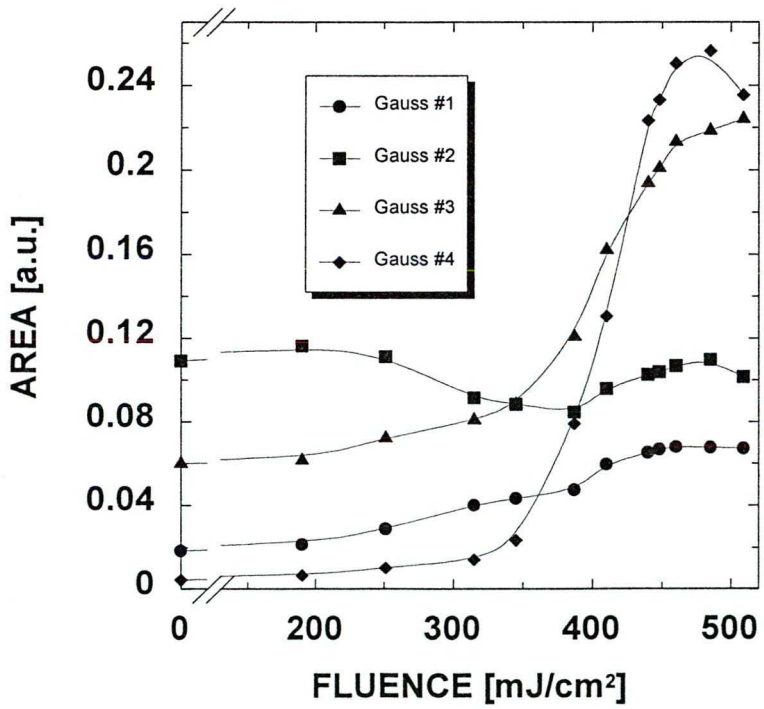

Fig. 30. The integrated peak area of Gaussian components after deconvolution of the absorption curves as a function of fluence. The four peaks are located at 0.7, 1.0, 1.6 and 2.6 eV (#1 to 4, respectvely), with minor variation of their exact position and width with fluence.

Fig. 31 shows the time evolution of the temperature on the surface and on the film—glass substrate interface at seven fluence values ranging from 190 to 500 mJ/cm^2. At single-pulse fluences below 190 mJ/cm^2, maximum surface temperatures remain below

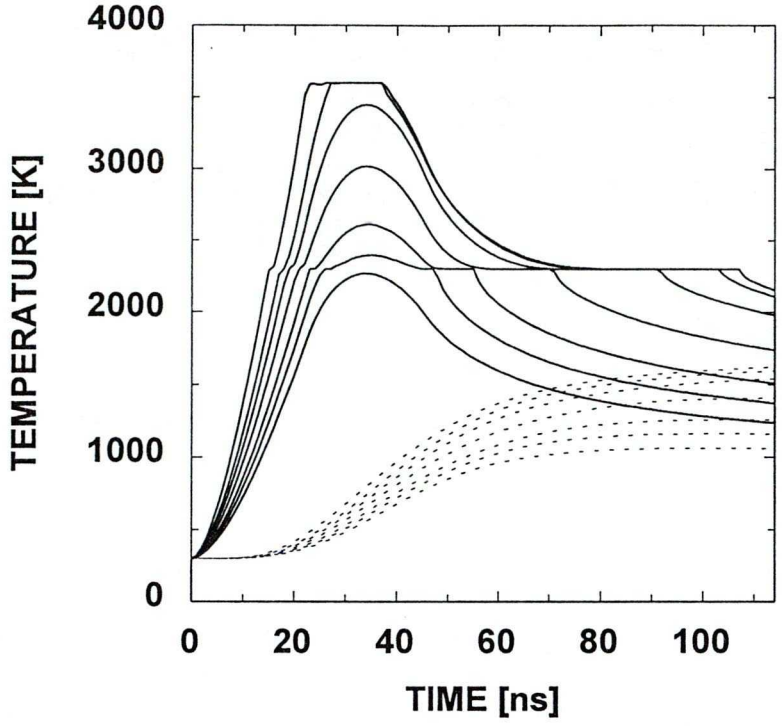

Fig. 31. The surface (solid lines) and interfacial (dashed lines) temperatures in ITO films irradiated with fluences of 190, 220, 250, 300, 350, 400 and 500 mJ/cm^2 (from bottom to top). The varying slope at 2300 K indicates the melting of ITO films, while the truncated top of the last two curves indicates the onset of ablation.

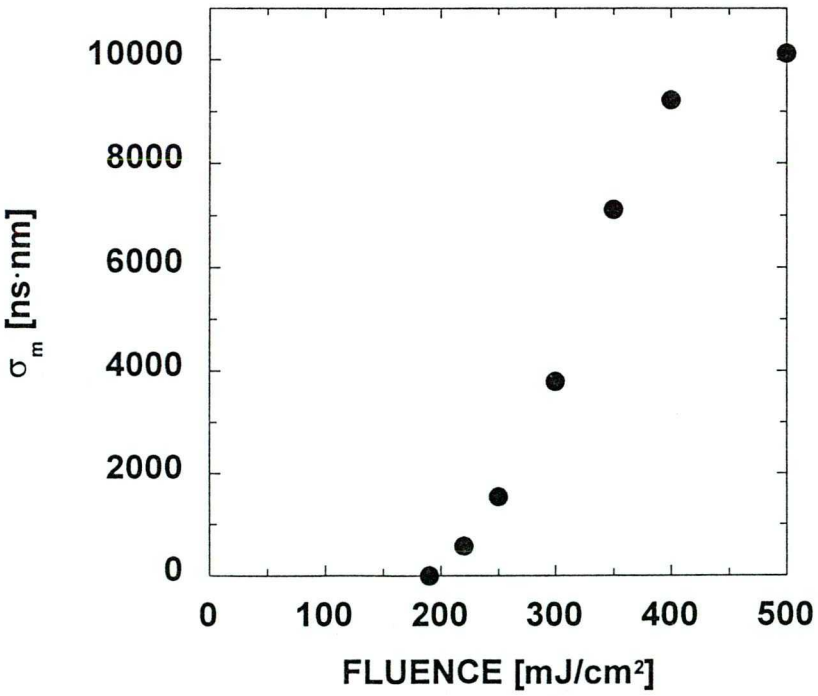

Fig. 32. σ_m as a function of processing laser fluence. The molten depth $d_m(t)$ obtained from temperature calculations was integrated with respect to time as $\sigma_m = \int d_m dt$.

the melting point. The model calculations predict the onset of melting between 190 and 200 mJ/cm^2, i.e. in the fluence domain corresponding precisely to the first unambiguous variations in the experimental optical spectra (Fig. 30). Increasing fluence results in higher surface temperatures, expanding molten volumes and increase in the lifetime of molten phase. As seen in Fig. 32, the rate of these changes is the highest between 250 and 350 mJ/cm^2. At even higher fluences, the processing efficiency decreases. The reason for this decay is that on reaching 3600 K, i.e. the evaporation temperature of ITO, a continuously increasing fraction of the injected energy is used for evaporation of the outermost surface layer. The model calculations indicate the onset of evaporation at around 400 mJ/cm^2, with still minor material losses up to 500 mJ/cm^2: the calculated ablation depth is 10 nm for 500 mJ/cm^2, which amounts to some 5% of the total molten depth, d_m.

Despite the approximations involved in the modelling, the results of the thermal calculations demonstrate that the principal effect induced by single-pulse processing in the 190—500 mJ/cm^2 fluence domain is deep melting in actual films. In light of these results, it is reasonable to assume that defects created in the molten phase and trapped upon resolidification are responsible for changes in the short-range chemical structure as revealed by optical and X-ray photoelectron spectroscopy. Since the total number of such defects is anticipated to depend on both the total molten volume and on the lifetime of the molten phase, the integral $\sigma_m = \int d_m dt$ has been calculated for the seven fluence values of Fig. 31. The dependence of σ_m on fluence is shown in Fig. 32. This anticipation finds indeed support in the striking similarity of Fig. 32. and curve #4 in Fig. 30.

3.5.5. Conclusions

Indium-tin oxide films of varying thicknesses within the limits of the thermal diffusion length possess different ablation characteristics due to the low heat conductivity of the glass substrate. With increasing film thickness the ablation depth decreases and the threshold fluence of layer-by-layer ablation shifts to higher values. A particularity of the thinner films is the possibility of complete removal of the film over the whole illuminated area with a single, low-fluence pulse, without massive thermal load of the substrate, providing a highly efficient and convenient means for one-step, large-area surface patterning.

4. Summary (theses)

4.1. Pulsed laser-induced ablation and transfer of thin metal films

By the critical analysis of ns-pulse induced laser transfer I showed that this process was not appropriate for micrometer resolution pattern production: high fluences resulting in melting or evaporation of the film material produced non-contiguous patterns with uncontrollable quality and dimensions, while low-fluence processing did not ensure good adhesion of the print patterns to the target substrate .

Although low-fluence, solid-phase *clean ablation* allows the removal of contiguous thin film patterns over the illuminated area, the transfer and especially the efficient deposition of these patterns is no longer achieved using such short laser pulses. For successful transfer, longer (sub-millisecond) pulses are necessary. I have demonstrated the feasibility of long-pulse laser transfer of tungsten thin films [T1-T6].

4.2. Laser microfabrication and monitoring system

Based on a diode-pumped Nd:YAG laser, I have constructed an electronically controlled experimental system which is capable to record in real-time the changes of the reflectivity and transmission of a thin film sample exposed to the laser radiation.

The bandwidth of the measurement of the optical transients is approx. 0.5 MHz. I have applied a special laser control scheme which allows the application of our laser with a modulation bandwidth above 50 kHz, overriding the factory-specified limitation of some 1 kHz. The processing power at the sample surface is electronically tunable between practically zero and 430 mW. The time shaping of the laser intensity, sample positioning, acquisition and processing of the optical data are managed by the same personal computer [T7, T8].

4.3. Dynamics of sub-millisecond laser pulse induced transfer of thin tungsten patterns

The dynamics of the process was followed by means of the laser microprocessing and monitoring system. The measured real-time transmission and reflection data was compared to result of numerical temperature calculations. I have shown that (i) the characteristic processes involved in long-pulse laser transfer start at well defined constant temperatures, regardless of the shape and duration of the laser pulse. (ii) With appropriate shaping of the second part of the processing pulse, on-site annealing of the deposited patterns can be attained improving its adherence to the target substrate. (iii) For these long laser pulses the conventional description of laser-induced transfer, which was based on a clear distinction between material removal, followed by its transfer and deposition, appropriate for ns-pulse processing, cannot be applied. In this case the thermal expansion is comparable with the gap width between the film and target faces, and, thus, the removal phase is strongly overlapping in space and time with the transfer and adherence steps [T7-T9].

4.4. Dynamics of laser-induced synthesis of ZnSe thin film patterns

I have demonstrated laser-induced synthesis of microcrystalline ZnSe films from multilayered elements.

The analysis of real-time reflectivity and transmission measurements has shown, that the overall process consists of three phases. The first one is fast intermixing between the film materials triggered by the melting of the selenium and, thereby, bound to exceeding a threshold temperature. The second phase is chemical reaction between Zn and

Se atoms, which transforms the unstable mixture into amorphous compound. Finally, the layer undergoes a relatively slow crystallization process. Upon increasing the processing power, the particular processes take place with higher rates.

The mechanism of this synthesis was investigated on the time scale ranging from one second down to few tens of microseconds. In this range I did not observe the\any saturation of the speed of the particular reactions with increasing heat injection rate, thus possibility of further shortening of the total processing times can be expected [T8].

4.5. Excimer laser ablation of transparent conductive thin films

I have shown that the differences in the thermal and mechanical properties of the film and the substrate are responsible for the variation of the ablation characteristics of thin tin oxide and indium-tin oxide films with varying thickness. As far as the film thickness does not exceed the thermal diffusion length corresponding to the actual laser pulse length, (1) the extensive heating of the film—substrate system or the fast resolidification of the molten layer may result in the decoupling of the film from the substrate, and (2) in the fluence range of the layer-by-layer evaporative ablation, the single-shot ablation depth depends on the film thickness [T10, T11].

Our comparative studies have revealed that the structural defects, which result in coloration and changes in the electrical properties of the indium-tin oxide films processed at fluences below the ablation threshold, are produced in the molten state of the material [T12, T13].

5. Acknowledgements

I am grateful to Dr. Tamás Szörényi, my thesis supervisor, for the common work, for his constant help and much discussion, and to Professor Zsolt Bor, head of the Department of Optics and Quantum Electronics & the Research Group on Laser Physics of the Hungarian Academy of Sciences, for the interest, encouragement and support I could enjoy during the past years. Other colleagues also kindly helped with cooperation and discussions, as well as technical or administrative assistance: in alphabetical order: Zsolt Geretovszky, Dr. Zoltán Gingl, Dr. Péter Heszler, Dr. Béla Hopp, Lóránd Kelemen, Professor Lucien Diego Laude, Dr. Péter Mogyorósi, Dr. Zsolt Tóth and Dr. József Vinkó.

I could not have worked without the technical and administrative background supplied by the Departments of Optics and Quantum Electronics and Experimental Physics, the Research Group on Laser Physics of the Hungarian Academy of Sciences and the Computer Center of the József Attila University. I am grateful to the Scientific Carreer Committee (TMB) of the Hungarian Academy of Sciences for a three-year scholarship. The activities described in this thesis were partially supported by the National Committee for Technical Development (OMFB) and the National Foundation for Scientific Research (OTKA I/3060 & F7529).

6. Appendix

Temperature calculations

In this section the basics of the numerical temperature calculations are briefly outlined. Details concerning the numerical (computational) implementations of the differential equations would be out of the scope of this work, only the general form of the applied thermal conductivity equation and the concepts of its simplification and application for special experimental cases are described here.

The heat flow equation can be written in the following general form:

$$\mathrm{div}[\kappa(T)\mathrm{grad}\,T]+Q(\mathbf{x},t)=\rho(T)c(T)\frac{\partial T}{\partial t},$$

where T, t, κ, ρ and c denote the temperature, time, thermal conductivity, density and specific heat of the film or the glass support, respectively. T is treated as a function of the space coordinates. In thin film processing, it is assumed that from one side the sample is limited by a plane, and for practical purposes, x and y are the spatial Cartesian coordinates and z is the one perpendicular to the sample surface (in all experimental arrangements discussed in the following part of this work, the beam axis is perpendicular to the processed surface). Q is the heat per unit volume and time generated in the system, due to the conversion of the absorbed light energy into heat upon laser irradiation. Also energy liberation upon chemical reactions can contribute to this source term. The material parameters, κ, ρ and c are functions of the temperature, and furthermore, since different materials or phases may be present in the volume of interest, they depend explicitly on the space coordinates. Although this dependence can not be described with continuous functions, the discretization schemes applied in numerical temperature calculations provide the possibility to take this dependencies into account at the interfaces (the finite difference schemes used for this work are much similar to that developed by Jain et al., see Ref. [53]). Heat transfer toward the ambient atmosphere, as well as radiative cooling of the surfaces were neglected because of their very small volume for the temperatures and illumination (or thermal relaxation) times in our experiments.

In many cases the actual experimental arrangements have special features, which provide significant simplifying conditions resulting in considerable reduction of the computation time. For example, when the spatial dimensions of the homogeneously illuminated processing area are much larger than the characteristic thermal diffusion length $l_\tau=\sqrt{4D\tau}$ in the heated material of thermal diffusivity $D=\frac{\kappa}{\rho c}$ corresponding to the illumination time τ, then lateral heat redistribution is not effective and, hence, derivatives with respect to x and y are zero. The problem can be solved by numerical integration of the following one-dimensional form of the above heat flow equation:

$$\frac{\partial}{\partial z}\left[\kappa(T)\frac{\partial T}{\partial z}\right]+I(z,t)\alpha(T)=\rho(T)c(T)\frac{\partial T}{\partial t}$$

where in addition to the quantities defined above, I(z,t) is the laser light intensity (i.e. power density) in depth z at time t and α(T) is the temperature dependent absorption

coefficient. Provided the laser light propagates toward increasing values of z, changes of I with respect to depth can be calculated using the differential Beer's law, i.e.

$$\frac{dI}{dz} = -\alpha I,$$

while the time dependence is incorporated through the temporal profile of the incident laser intensity at the sample surface, $I_0(t)$, as

$$I(0,t) = (1-R)I_0(t),$$

where R is the reflectivity of the surface at the wavelength of the illumination. Sometimes the explicit temperature dependence of α can be neglected [94], then constant α is used and the intensity profile in depth can be written as

$$I(z,t) = I_0(t)(1-R)e^{-\alpha z}.$$

Another important example for reduction of the dimensionality of the system is the case of irradiation with TEM_{00} laser beam. Due to the cylindrical symmetry, the system is insensitive to rotation around the optical axis (i.e. z) and thus all derivatives with respect to the angular coordinate are zero (of course, in this case the system can be handled more easily in a cylindrical system of coordinates).

For longer illumination with focused laser pulses, the system can not be further simplified, since both lateral and perpendicular components of the heat flow are significant.

Phase transitions were generally considered in the calculations, and whenever it was available, temperature dependent data were used for the molten phase, as well. The effects of material displacement (thermal expansion, volume change upon melting, the *ablation* itself, etc.) were however not included, even though they were clearly observable.

In case of the calculation of the temperatures of a thin film, the appearance of the vapour phase causes usually a stiff problem with shielding from the laser light and the strength of the thermal coupling of the vapour with the underlying substances, thus temperatures above the boiling point, i.e. the ablated state of the matter can be interpreted with very careful definition of the material properties and boundary conditions. Nevertheless, no such problems arise with the detection of the onset of evaporation.

References

[1] D. J. Ehrlich, J. Y. Tsao, Editors: Laser Microfabrication: Thin Film Processes and Lithography (Academic Press Inc., 1989).

[2] D. Bäuerle: Chemical Processing with Lasers (Springer Series in Materials Science, v. 1, Springer-Verlag, Berlin—Heidelberg, 1986).

[3] Zs. Geretovszky, K. Bali, A. Tóth and T. Szörényi, Thin Solid Films, **241**, 67 (1994).

[4] K. Bali, T. Szörényi, M.R. Brook, and G.A. Shafeev, Appl. Surf. Sci., **69**, 75 (1993).

[5] R. R. Krchnavek, H. H. Gilgen, R. M. Osgood, Jr., J. Vac. Sci. Technol. **B 2**, 641 (1984).

[6] G. J. Fisanick, M. E. Gross, J. B. Hopkins, M. D. Fennell, K. J. Schnoes and A. Katzir, J. Appl. Phys. **57**, 1139 (1985).

[7] Jun-Ying Zhang; H. Esrom, Appl. Surf. Sci. **54**, 465 (1992).

[8] P. B. Shrivastva, C. Harteveld, C. A. Boose, B. H. Kolster, Appl. Surf. Sci. **51**, 165 (1991).

[9] L. L. Burns, Laser Focus **16** (1980) 48, 50, 54.

[10] V. P. Veiko, I. M. Karpman, M. N. Libenson, E. B. Yakovlev, Kvantovaya Elektronika, **9** (1982) 2167.

[11] V. P. Veiko, "Lazernaya obrabotka pl'yonochnich elementov" (1986).

[12] M. I. Cohen, B. A. Unger and J. F. Milkosky, The Bell System Technical Journal **40** (1968) 395.

[13] E. F. Krimmel, A. G. K. Lutsch, L. Hoffmann, C. Weyrich, J. Appl. Phys. **55** (1984) 1617.

[14] V. J. Zaleckas, in *Conference on Laser and Electrooptical Systems*. (Digest of technical papers.) New York, NY, USA: IEEE (1976) p. 8.

[15] O. T. Masopust, Jr., M. A. Saifi, Western Electric Engineer **21** (1977) 48.

[16] M. A. Saifi, O. T. Masopust ,Jr., IEEE Journal of Quantum Electronics **QE-12** (1976) 120.

[17] G. Ripka, I. Hajdu: "Hybridschaltungen: Dünn- und Dickschichttechnologie" (Akadémiai Kiadó, Budapest, 1987).

[18] P. Morillon, private communication.

[19] J. S. Bakos, M. A. Kedves, J. Szigeti, AIP Conf. Proc., 1995 (no. 329), p. 357.

[20] I. Sánta, in *Winter School on Quantum Electronics*, Esztergom, 1992.

[21] G. Veres, P. N. Ignácz, B. Kardon, G. Kocsis, J. S. Bakos, Nucl. Instr. Meth. Phys. Res. **B71** (1992) 221.

[22] M. Toulemonde, J. C. Muller and R. Stuck, Transactions of the ASME. Journal of Solar Energy Engineering, **108** (1986) 102.

[23] D. B. Chrisey, G. K. Hubler, Editors: Pulsed Laser Deposition of Thin Films (John Wiley & Sons, Inc. 1994).

[24] "Explosive Welding", *Mech. Eng.* (May 1978) 28.

[25] M. B. Frish and P. Nebolsine, "Surface Coating and Alloying by Laser Induce Heat and Pressure", Final Report, NSF Grant No. DMR-8260087 (1983).

[26] D. E. Alexander, G. S. Was and F. J. Mayer, J. Mat. Sci. **23,** 2181 (1988).

[27] J. Bohandy, B. F. Kim and F. J. Adrian, J. Appl. Phys. **60**, 1538 (1986).

[28] Z. Tóth and T. Szörényi, Appl. Phys. **A 52,** 273 (1991).

[29] Z. Tóth and T. Szörényi, Thin Solid Films **245** (1994) 40.

[30] J.-Y. Zhang, H. Esrom and I. W. Boyd, talk on the E-MRS 1995 Spring Meeting, Conference on Laser Ablation.

[31] H. Esrom, private communication.

[32] J. A. Greer and T. E. Parker, in *Excimer Beam Applications* (Proc. SPIE 998, 1988) p. 113.
J. A. Greer, T. E. Parker, M. Rotschild and D. J. Ehrlich, in Proceedings of the 41st Annual Frequency Symposium (New York, NY, USA: IEEE 1987), p.351

[33] T. Sameshima, Appl. Surf. Sci. **96-98** (1996) 352.

[34] P. Mogyorósi, T. Szörényi, K. Bali, Zs. Tóth and I. Hevesi, Appl. Surf. Sci. **36** (1989) 157.

[35] E. Fogarassy, C. Fuchs, F. Kerherve, G. Hauchecorne and J. Perriere, J. Mater. Res. **4,** 1082 (1989).

[36] R. J. Baseman, J. C. Andreshak, MRS Proc. No. **100** (1989) 627.

[37] F. J. Adrian, J. Bohandy, B. F. Kim and A. N. Jette, J. Vac. Sci. Technol. **B 5,** 1490 (1987).

[38] J. Bohandy, B. F. Kim, F. J. Adrian, and A. N. Jette, J. Appl. Phys. **63,** 1158 (1988).

[39] R. J. Baseman, A. Gupta, R. C. Sausa and C. Progler, in *Laser and Particle-Beam Chemical Processing for Microelectronics,* edited by D. J. Ehrlich, G. S. Higashi, and M. M. Oprysko (MRS, Pittsburg, PA, 1988), Vol **101**, p. 237.

[40] R. J. Baseman, N. M. Froberg, J. C. Andreshak, Z. Schlesinger, Appl. Phys. Lett. **56** (1990) 1412.

[41] E. Matthias, J. Siegel, S. Petzoldt, M. Reichling, H. Skurk, O. W. Käding, E. Neske, This Solid Films, **254** (1995) 139.

[42] E. Matthias, M. Reichling, J. Siegel, O. W. Käding, S. Petzoldt, H. Skurk, P. Bizenberger, E. Neske, Appl. Phys. **A58** (1994) 129.

[43] E. Matthias, M. Reichling, J. Siegel, O. W. Käding, S. Petzoldt, H. Skurk, in: *Laser Ablation: Mechanisms and Applications—II.* AIP Conf. Proc. No. 288., AIP Press, New York (1994) 305.

[44] A. Rosenfeld and E. E. B. Campbell, Appl. Surf. Sci. **96-98** (1996) 439.

[45] Z. Tóth, private communication.

[46] Z. Tóth, T. Szörényi and A. L. Tóth, Appl. Surf. Sci. **69** (1993) 317.

[47] Z. Tóth, J. Solis, C. N. Afonso, F. Vega and T. Szörényi, Appl. Surf. Sci. **69** (1993) 330.

[48] J. Farkas, [Laser beam assisted repair of chrome-glass lithographic masks used in semiconductor technology], Thesis, Technical University of Budapest (1989)

[49] M. Thuillard and M. Von Allmen, Laser produced Ti/Ti-oxide thin film structures, Appl. Phys. Lett. **47**, 936 (1985)

[50] M. Thuillard and M. Von Allmen, Laser produced percolation structures, Appl. Phys. Lett. **48**, 1045 (1986)

[51] V. Craciun, D. Craciun, N. Chitica and I. N. Michailescu, Appl. Surf. Sci. **54** (1992) 362.

[52] DPY 321 Diode Pumped Nd:YAG laser, "Users Manual"

[53] A. K. Jain, V. N. Kulkarni and D. K. Sood, Appl. Phys. **25,** 127 (1983).

[54] R. Andrew, M. Ledezma, M. Lovato, M. Wautelet and L. D. Laude, Appl. Phys. Lett. **35**, 418 (1979).

[55] L. D. Laude: in Laser Processing and Diagnostics, ed. D. Bäuerle, Springer Ser. Chem. Phys. **39** (Springer Berlin, Heidelberg, 1984) p. 355-365.

[56] L. D. Laude, Mat. Res. Soc. Symp. Proc. **23** (Elsevier, New York, 1984) p. 611-620.

[57] L. D. Laude, Prog. Cryst. Growth & Charact. **10**, 141 (1984).

[58] F. Catalina, C. N. Afonso, R. Serna and F. Vega, Surf. Sci. **251/252**, 1006 (1991).

[59] M. von Allmen, S. S. Lau, M. Maenpaa, B. Y. Tsaur, Appl. Phys. Lett. **36** (1980) 205.

[60] T. Szörényi, J. Kovács, E. Szil, Revue Roumanie de Physique **31** (1986) 1079.

[61] J. M. Poate, H. J. Leamy, T. T. Sheng, G. K. Celler, Appl. Phys. Lett. **33** (1978) 918.

[62] E. D'Anna, G. Leggieri, A. Luches, V. Nassisi, A. Perrone, G. Majni, P. Mengucci, Appl. Surf. Sci. **36** (1989) 500.

[63] M. von Allmen, M. Wittmer, Appl. Phys. Lett. **34** (1979) 68.

[64] H. S. Lee, G. J. Wolga, J. Electrochem. Soc. **137** (1990) 684.

[65] E. D'Anna, A. V. Drigo, G. Leggieri, A. Luches, G. Majni, P. Mengucci, Appl. Phys. **A50** (1990) 411.

[66] K. Kolev and L. D. Laude, Appl. Surf. Sci., **54**, 385 (1992).

[67] CRC handbook of chemistry and physics: a ready-reference book of chemical and physical data, Ed.: David R. Lide., 72nd ed. (1991-92 ed.) Boca Raton, FL.: CRC Press, 1991., p. E-101

[68] F. Hanus, M. Wautelet, Appl. Surf. Sci. **43** (1989) 271.

[69] E. E. Marinero, in Proceedings of *Beam—Solid Interactions and Transient Processes* Symposium, ed. by M. O. Thompson, S. T. Picraux, J. S. Williams; Pittsburgh, USA. Mater. Res. Soc. (1987) 237.

[70] D. J. Gravesteijn, H. M. van Tongeren, M. Sens, T. Bertens, C. J. van der Poel, Appl. Optics **26** (1987) 4772.

[71] "The Red Book" of SONY

[72] K. Badeker, Ann. Phys. (Leipzig) **22** (1907) 749.

[73] P. Kathirgamanathan, Intern. J. of Electronics **77** (1994) 937.

[74] K. L. Chopra, S. Major, and D. K. Pandya, Thin Solid Films **102**, 1 (1983).

[75] J. Molloy, P. Maguire, S. J. Laverty, J. A. McLaughlin, J. Electrochem. Soc. **142** (1995) 4285.

[76] R. R. Kunz, M. Rotschild, D. J. Ehrlich, Appl. Phys. Lett. **54** (1989) 1631. R. R. Kunz, M. Rotschild, D. J. Ehrlich, in *Laser- and Particle-Beam Chemical Processes on Surfaces Symposium*, ed. by A. W. Johnson, G. L. Loper, T. W. Sigmon (Mat. Res. Soc. Pittsburgh, USA, 1989) p. 447.

[77] Zs. Geretovszky, L. Kelemen, T. Szörényi, private communication.

[78] S. Nakano, T. Matsuoka, S. Kiyama, H. Kawata, N. Nakamura, Y. Nakashima, S. Tsuda, H. Nishiwaki, M. Ohnishi, I. Nagaoka, Y. Kuwano, Jap. J. Appl. Phys. Part 1, **25** (1986) 1936.

[79] J. G. Lunney, R. R. O'Neill, and K. Schulmeister, Appl. Phys. Lett. **59** (1991) 647.

[80] V. N. Koinkar and S. B. Ogale, Thin Solid Films **206** (1991) 259.

[81] F. Meringdal and H. Slinde, in *Excimer Lasers and Applications III* (Proc. SPIE Vol. **1503**, 1991), 292-298.

[82] H. Galindo, A. B. Vincent, J. C. Sánchez-R. and L. D. Laude, J. Appl. Phys. **74** (1993) 645.

[83] M. Eyett and D. Bäuerle, Appl. Phys. Lett. **51** (1987) 2054

[84] M. J. Wheeler, Brit. J. Appl. Phys. **16** (1965) 365.

[85] Y. S. Touloukian, R. W. Powell and C. Y. Ho, Thermophysical Properties of Matter (IFI/Plenum New York 1973).

[86] E. H. P. Cordfunke, E. F. Westrum, jr., J. Phys. Chem. Solids **53** (1992) 361.

[87] Comprehensive inorganic chemistry. Ed.: J. C. Bailar, Jr., 1st ed., Oxford, Pergamon Press; N.Y. (1973) p. 1092.

[88] R. L. Weiher, R. P. Ley, J. Appl. Phys. **37** (1966) 299.

[89] J. C. C. Fan, and J. B. Goodenough, J. Appl. Phys. **48**, 3524 (1977).

[90] R. Oesterlein, and H.—J. Krokoszinski, Thin Solid Films **175**, 241 (1989).

[91] S. Major, S. Kumar, M. Bhatnagar, and K. L. Chopra, Appl. Phys. Lett. **49**, 394 (1986).

[92] R. Banerjee, S. Ray, N. Basu, A. K. Batabyal, and A. K. Barua, J. Appl. Phys. **62**, 912 (1987).

[93] T. Minami, H. Sato, H. Nanto, and S. Takata, Thin Solid Films **176**, 277 (1989).

[94] R. W. Wood: Physical Optics (New York, 1924)

Thesis references

[T1] Zs. Tóth, Z. Kántor, P. Mogyorósi and T. Szörényi, "Surface Patterning by Pulsed Laser-Induced Transfer of Metals and Compounds" in *Laser Assisted Processing II,* edited by L. D. Laude (Proc. SPIE Vol. **1279**, 1990), p. 150.

[T2] Z. Kántor, Zs. Tóth, T. Szörényi, "Laser-Induced Forward Transfer: The Effect of Support-Film Interface and Film-to-Substrate Distance on Transfer", Appl. Phys. A **54** (1992) 170.

[T3] Z. Tóth, B. Hopp, Z. Kántor, F. Ignácz, T. Szörényi and Zs. Bor, "Dynamics of excimer laser ablation of thin tungsten films studied by fast photography" in *Laser Materials Processing: Industrial and Microelectronic Applications* (Proc. SPIE **2207**, 1994) p. 776.

[T4] Z. Tóth, B. Hopp, Z. Kántor, F. Ignácz, T. Szörényi, and Z. Bor, "Dynamics of excimer laser ablation of thin tungsten films films as followed by ultrafast photography", Appl. Phys. **A 60** (1995) 431.

[T5] T. Szörényi, Z. Tóth and Z. Kántor, "Surface patterning by an improved laser-induced forward transfer (LIFT) technique" in *Thin Films and Microstructures*, Ian W. Boyd, Editor, Proc. SPIE Vol. **2045** (1994) 126.

[T6] Z. Kántor, Z. Tóth, T. Szörényi, A. L. Tóth, "Deposition of micrometer-sized tungsten patterns by laser transfer technique", Appl. Phys. Lett. **64**, 3506 (1994).

[T7] Z. Kántor and T. Szörényi, "Dynamics of long-pulse laser transfer of micrometer-sized metal patterns as followed by time-resolved measurements of reflectivity and transmittance", J. Appl. Phys. **78** (1995) 2775.

[T8] Z. Kántor and L. D. Laude, "Dynamics of Laser-Induced Synthesis of ZnSe", J. Appl. Phys. **80** (1995) 662.

[T9] Z. Kántor, Z. Tóth and T. Szörényi, "Metal Pattern Deposition by Laser-Induced Forward Transfer", Appl. Surf. Sci. **86** (1995) 196.

[T10] T. Szörényi, Z. Kántor and L. D. Laude, "Atypical characteristics of KrF excimer laser ablation of indium-tin oxide films", Appl. Surf. Sci. **86** (1995) 219.

[T11] T. Szörényi, Z. Kántor and L. D. Laude, "Unusual features of laser ablation of supported thin films" in *Laser Materials Processing: Industrial and Microelectronic Applications*, Eckhard Beyer, Maichi Cantello, Aldo V. la Rocca, Lucien D. Laude, Flemming O. Olsen, Gerd Sepold, Editors (Proc. SPIE **2207**, 1994), p. 590.

[T12] T. Szörényi, L. D. Laude, I. Bertóti, Z. Kántor and Zs. Geretovszky, "Excimer laser processing of indium-tin oxide films: an optical investigation", J. Appl. Phys. **78** (1995), 6211.

[T13] T. Szörényi, L. D. Laude, I. Bertóti, Zs. Geretovszky and Z. Kántor, "Low-Fluence Excimer Laser Irradiation-Induced Defect Formation in Indium-Tin Oxide Films", Appl. Surf. Sci. **96-98** (1996) 363.

Content